Comprehensive Impedance Analysis of DFIG-Based Wind Farms Considering Dynamic Couplings

Jinlong Wang, *Student Member, IEEE*, Peng Wang, *Member, IEEE*, Haoran Zhao, *Senior Member, IEEE*, and Futao Yang

***Abstract*—Existing wind farm impedance analyzes using aggregated impedance models neglect the influence mechanisms of dynamic couplings between wind farm control (WFC), wind turbines, and collector lines on system stability. This article proposes a novel comprehensive impedance model (CIM) for the wind farm based on the doubly-fed induction generator (DFIG), considering multiple dynamic couplings for thorough impedance analysis. At the DFIG level, small-signal characteristics of rotor speed are introduced into the impedance model to reflect couplings between mechanical and electromagnetic dynamics. Meanwhile, at the wind farm level, couplings between the WFC and DFIGs are represented as a current source controlled by voltage and current perturbations at the wind farm point of common coupling (PCC), connected in parallel with the original DFIG impedance. Since the PCC voltage and current are associated with all DFIGs and collector lines, this controlled source effectively captures their couplings. Analysis with CIM reveals that considering mechanical dynamics improves the accuracy of DFIG impedance in the low-frequency band, while the WFC affects the impedance characteristics of the wind farm in the full-frequency range. Moreover, excessively large WFC proportional-integral parameters can lead to system destabilization. Simulation and experimental results confirm the validity of the CIM and its precise application in stability analysis.**

***Index Terms*—Comprehensive impedance model (CIM), doubly-fed induction generator (DFIG), dynamic coupling, mechanical dynamic, small-signal stability, wind farm control (WFC).**

I. INTRODUCTION

THE integration of wind power increases the utilization of power electronics and enhances controllability in modern power systems. However, dynamic interactions between wind farms and the grid significantly impact system stability and reliability, leading to frequent stability issues [1]. Notably, numerous sub/super-synchronous oscillations in North China and the Electric Reliability Council of Texas (ERCOT) region, along with emerging low-frequency oscillations, have resulted in adverse consequences, such as generator damage and disconnection of wind farms [2], [3].

In this context, impedance analysis is a practical methodology for assessing the small-signal stability of grid-connected wind farm systems [4]. Fig. 1 illustrates the overall structure of a wind farm [5]. There are couplings between mechanical and electromagnetic dynamics within the wind turbine (WT). Interactive couplings between the wind farm control (WFC) and WTs also exist, leading to further couplings between WTs and collector lines. However, in current wind farm impedance analyzes based on aggregated impedance models, mechanical dynamics and WFC dynamics are commonly ignored [6].

As the predominant type of WT, the doubly-fed induction generator (DFIG) has attracted significant attention regarding its impedance characteristics [7], [8], [9], [10], [11]. The DFIG impedance models for analyzing sub/super-synchronous or high-frequency oscillations have been developed in [9] and [10]. Furthermore, the investigation of how DFIG electrical and control parameters affect system stability is presented in [11]. While several studies have delved into DFIG impedance analysis, their primary focus has been on electromagnetic dynamics. These studies generally assume a constant rotor speed, thereby neglecting mechanical dynamics. Notably, the electrical and mechanical subsystems of the DFIG are interconnected [12]. Disturbances in either subsystem can induce changes in DFIG impedance characteristics. Consequently, a DFIG impedance model lacking the dynamics of the mechanical subsystem will inaccurately represent impedance characteristics and hinder the influence analysis of couplings between mechanical and electromagnetic dynamics on system stability.

The WFC implements a specific control strategy to dispatch power references to each WT, with the aim of controlling the output power at the point of common coupling (PCC) of the wind farm [13]. The transmission of power control signals induces couplings between the WFC and WTs, enabling small-signal perturbations to be exchanged among them during stability analysis. Therefore, WFC dynamics will affect wind farm impedance characteristics through these couplings. However, existing WFC research mainly focuses on optimizing power control strategies to improve power tracking accuracy and power output smoothness [14], [15]. There is a noticeable absence of studies examining the impact of dynamic couplings introduced by the WFC on the stability of the grid-connected wind farm system. Most wind farm impedance modeling assumes the decoupling of WTs from each other and from collector lines, resulting in simplified aggregation methods, such as series-parallel connection of single WT impedance [16] or multi-WT equivalence [17]. Therefore,

Manuscript received 31 October 2023; revised 29 February 2024 and 21 May 2024; accepted 28 June 2024. Date of publication 2 July 2024; date of current version 12 December 2024. Recommended for publication by Associate Editor M. S. ElMoursi. *(Corresponding author: Haoran Zhao.)*

The authors are with the School of Electrical Engineering of Shandong University, Jinan 250061, China (e-mail: 202220673@mail.sdu.edu.cn; p.wang@sdu.edu.cn; hzhao@sdu.edu.cn; 202120611@mail.sdu.edu.cn).

Color versions of one or more figures in this article are available at https://doi.org/10.1109/TPEL.2024.3422033.

Digital Object Identifier 10.1109/TPEL.2024.3422033

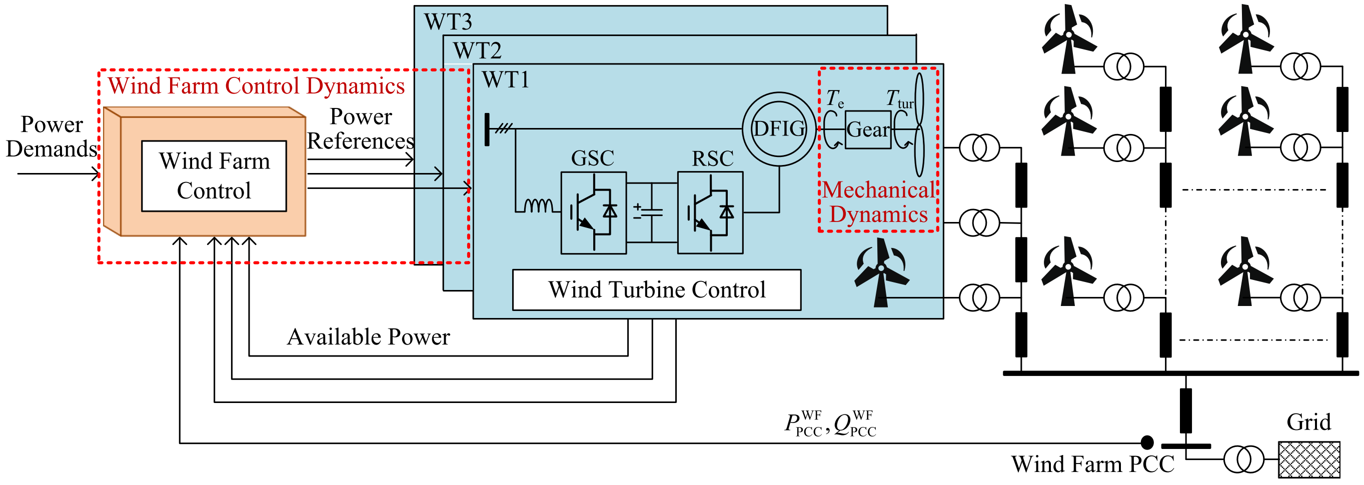

Fig. 1. Overall of the DFIG-based wind farm.

it is imperative to promptly formulate a fully integrated impedance model that accounts for these dynamic couplings as a standardized framework for wind farm impedance analysis.

As interactions between wind farms and grids intensify, multiple dynamic couplings significantly influence system stability. Moreover, these multiscale dynamic couplings in both temporal and spatial domains complicate propagation paths of small-signal perturbations, posing challenges to impedance modeling [18]. To address these problems, this article develops a comprehensive impedance model (CIM) for DFIG-based wind farms to represent impedance characteristics involving multiple dynamic couplings accurately. The CIM is rigorously validated for correctness and is intended to serve as the foundational model for subsequent studies related to system stability. The main innovations can be summarized as follows.

1) By analyzing the small-signal characteristics of rotor speed within the context of a wind energy conversion system, a full-frequency impedance model for the DFIG in the dq-frame is derived. This impedance model accurately captures the couplings between mechanical and electromagnetic dynamics within the DFIG.
2) The impact of the WFC dynamics can be represented by a controlled current source connected in parallel with the original DFIG impedance. The control variables consist of voltage and current perturbations at the wind farm PCC, effectively reflecting the couplings between the WFC, DFIGs, and collector lines. Consequently, the CIM of the wind farm is constructed based on the node admittance matrix.
3) The frequency characteristics of the CIM are analyzed, demonstrating the effect of multiple dynamic couplings on wind farm impedance and its superiority in stability analysis compared to the simplified impedance. In addition, an investigation is conducted to assess the influence of WFC proportional-integral (PI) parameters on system stability.

The rest of this article is organized as follows. Section II presents the full-frequency DFIG impedance model incorporating mechanical dynamics. Section III develops the wind farm CIM considering WFC dynamics. Section IV analyzes the impedance characteristics and influencing factors of the wind farm CIM. Section V shows the simulation and experimental verification. Finally, Section VI concludes this article.

II. DFIG IMPEDANCE MODELING CONSIDERING MECHANICAL DYNAMICS

A typical structure of the DFIG based on the wind energy conversion system within Fig. 1 is indicated in Fig. 2. Both the grid-side converter (GSC) and the rotor-side converter (RSC) adopt vector-oriented control. The power references for RSC control are provided by the WFC. The vector $\boldsymbol{x}=[x_\mathrm{d}, x_\mathrm{q}]^\mathrm{T}$ denotes the d-axis and q-axis components of any variable in the dq-frame, e.g., $\boldsymbol{u}_\mathrm{s}$ and $\boldsymbol{u}_\mathrm{r}$ are the stator and rotor voltages, $\boldsymbol{i}_\mathrm{s}$ and $\boldsymbol{i}_\mathrm{r}$ are the stator and rotor currents, $\boldsymbol{u}_\mathrm{g}$ and $\boldsymbol{i}_\mathrm{g}$ are the GSC voltage and current, and $\boldsymbol{i}_\mathrm{t}$ is the total current at the DFIG PCC. The current direction is displayed in Fig. 2.

The impedance transformation between different frames implies that the impedance is equivalent in all frames [19]. Since DFIG control operates in the dq-frame, this article derives the wind farm CIM in this frame. DFIG impedance modeling entails three distinct parts, as marked in Fig. 2. The interconnection between mechanical and electrical subsystems is mainly manifested through the rotor speed. Therefore, a small-signal model of rotor speed will be developed to account for mechanical dynamics, giving rise to differences in impedance derivation for both the generator and RSC parts compared to the existing impedance. In addition, it is important to note upfront that the phase-locked loop (PLL) dynamics result in two dq-frames within the DFIG system: one defined by the DFIG PCC voltage as the local grid dq-frame and another defined by the PLL as the control system dq-frame [19]. Assuming $\boldsymbol{x} = \boldsymbol{X} + \Delta\boldsymbol{x}$, where the capital letter $\boldsymbol{X}$ represents the steady-state value and $\Delta\boldsymbol{x}$ denotes the small-signal perturbation. The superscript "s" indicates variables in the local grid dq-frame, while the superscript "c" indicates variables in the control system dq-frame. According to the PLL structure shown in Fig. 2, the transfer function for $\Delta\boldsymbol{x}$ between two dq-frames can be

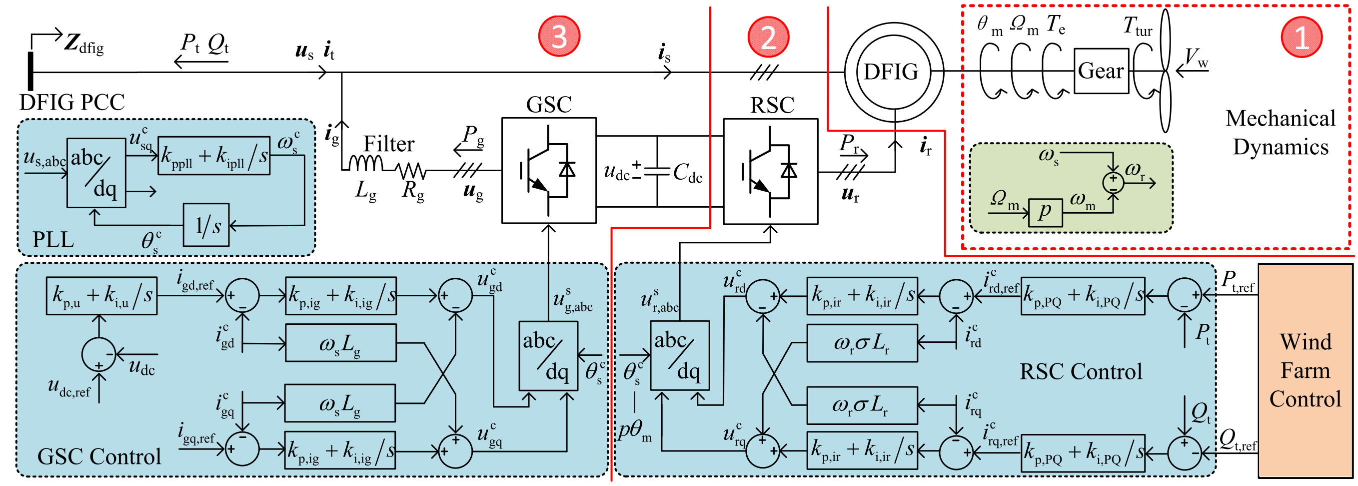

Fig. 2. Schematic of the DFIG based on the wind energy conversion system.

written as

$$\Delta \boldsymbol{x}^{\text{c}} = \boldsymbol{Z}_{\text{x}} \Delta \boldsymbol{u}_{\text{s}}^{\text{s}} + \Delta \boldsymbol{x}^{\text{s}} \tag{1}$$

$$\boldsymbol{Z}_{\text{x}} = \begin{bmatrix} 0 & Z_{\text{pll}} X_{\text{q}}^{\text{s}} \\ 0 & -Z_{\text{pll}} X_{\text{d}}^{\text{s}} \end{bmatrix}, \ Z_{\text{pll}} = \frac{s k_{\text{ppll}} + k_{\text{ipll}}}{s^2 + s U_{\text{sd}}^{\text{s}} k_{\text{ppll}} + U_{\text{sd}}^{\text{s}} k_{\text{ipll}}} \tag{2}$$

where s is the complex frequency in the Laplace transform. $\boldsymbol{Z}_{\text{x}}$ corresponds to $\boldsymbol{Z}_{\text{us}}$, $\boldsymbol{Z}_{\text{ur}}$, $\boldsymbol{Z}_{\text{it}}$, $\boldsymbol{Z}_{\text{ir}}$, $\boldsymbol{Z}_{\text{ug}}$, and $\boldsymbol{Z}_{\text{ig}}$ in sequence when $\boldsymbol{x}$ is $\boldsymbol{u}_{\text{s}}$, $\boldsymbol{u}_{\text{r}}$, $\boldsymbol{i}_{\text{t}}$, $\boldsymbol{i}_{\text{r}}$, $\boldsymbol{u}_{\text{g}}$, and $\boldsymbol{i}_{\text{g}}$.

A. Impedance Modeling of Mechanical Subsystem and Generator

The aerodynamic model represents power extraction of the rotor by calculating the mechanical torque T_{tur}, as follows:

$$T_{\text{tur}} = \frac{1}{2} \pi \rho r^3 V_{\text{w}}^2 C_{\text{T}}(\lambda, \beta) \tag{3}$$

where ρ is the air density, r is the blade length, V_{w} is the average wind speed, and $C_{\text{T}}(\lambda, \beta)$ is the torque coefficient. Specially, $\lambda = r\Omega_{\text{tur}}/V_{\text{w}}$ denotes the tip speed ratio, where Ω_{tur} is the mechanical angular velocity. The fixed pitch control is adopted with a constant pitch angle of $\beta = 0$. Meanwhile, the relationship between C_{T} and λ is quadratically fitted by the least squares method. $C_{\text{T}}(\lambda, \beta)$ can be expressed as

$$C_{\text{T}}(\lambda) = c_2 \lambda^2 + c_1 \lambda + c_0. \tag{4}$$

The small-signal characteristics of the DFIG are analyzed assuming a constant wind speed. Consequently, applying small-signal linearization to (3) gives the relationship between ΔT_{tur} and $\Delta \Omega_{\text{tur}}$, as follows:

$$\Delta T_{\text{tur}} = \frac{c_1 \pi \rho r^4 V_{\text{w}} + 2 c_2 \pi \rho r^5 \Omega_{\text{tur}}}{2} \Delta \Omega_{\text{tur}}. \tag{5}$$

The electromagnetic torque T_{e} associated with stator and rotor currents can be calculated as

$$T_{\text{e}} = \frac{3}{2} p L_{\text{m}} \left(-i_{\text{sd}}^{\text{s}} i_{\text{rq}}^{\text{s}} + i_{\text{sq}}^{\text{s}} i_{\text{rd}}^{\text{s}} \right) \tag{6}$$

where p is the number of pole pairs and L_{m} is the excitation inductance. Therefore, the linearization of (6) can yield

$$\Delta T_{\text{e}} = \frac{3}{2} p L_{\text{m}} \left(-I_{\text{rq}}^{\text{s}} \Delta i_{\text{sd}}^{\text{s}} + I_{\text{rd}}^{\text{s}} \Delta i_{\text{sq}}^{\text{s}} + I_{\text{sq}}^{\text{s}} \Delta i_{\text{rd}}^{\text{s}} - I_{\text{sd}}^{\text{s}} \Delta i_{\text{rq}}^{\text{s}} \right). \tag{7}$$

The gearbox makes the shaft more slender, resulting in mechanical stiffness comparable to electrical stiffness [20]. Moreover, the shaft stiffness is lower, and the generator is significantly lighter than the turbine. Therefore, a two-mass mechanical model is utilized to represent the drive train, achieving a balance between stability analysis and model complexity. With all amplitude variations considered to be in the high-speed shaft, the motion equations of the DFIG is

$$\begin{aligned} N J_{\text{t}} \frac{d\Omega_{\text{tur}}}{dt} &= \frac{T_{\text{tur}}}{N} - N D_{\text{t}} \Omega_{\text{tur}} - T_{\text{tm}} \\ J_{\text{m}} \frac{d\Omega_{\text{m}}}{dt} &= T_{\text{e}} - D_{\text{m}} \Omega_{\text{m}} + T_{\text{tm}} \\ \frac{dT_{\text{tm}}}{dt} &= K_{\text{tm}} (N\Omega_{\text{tur}} - \Omega_{\text{m}}) + D_{\text{tm}} \left(N \frac{d\Omega_{\text{tur}}}{dt} - \frac{d\Omega_{\text{m}}}{dt} \right) \end{aligned} \tag{8}$$

where N is the gearbox ratio, J_{t} and J_{m} are the two-mass mechanical inertia, D_{t} and D_{m} are the friction coefficients. The stiffness coefficient K_{tm} and damping coefficient D_{tm} define the flexible coupling between the two-mass. The generator angular velocity Ω_{m} is related to the rotor speed ω_{m} by $\Omega_{\text{m}} = \omega_{\text{m}}/p$. Therefore, the small-signal linearization and Laplace transform of (8) are performed as

$$\begin{aligned} s N J_{\text{t}} \Delta \Omega_{\text{tur}} &= \frac{1}{N} \Delta T_{\text{tur}} - N D_{\text{t}} \Delta \Omega_{\text{tur}} - \Delta T_{\text{tm}} \\ \frac{s J_{\text{m}}}{p} \Delta \omega_{\text{m}} &= \Delta T_{\text{e}} - \frac{D_{\text{m}}}{p} \Delta \omega_{\text{m}} + \Delta T_{\text{tm}} \\ s \Delta T_{\text{tm}} &= (N K_{\text{tm}} + s N D_{\text{tm}}) \Delta \Omega_{\text{tur}} - \frac{K_{\text{tm}} + s D_{\text{tm}}}{p} \Delta \omega_{\text{m}}. \end{aligned} \tag{9}$$

Therefore, the small-signal model of rotor speed can be expressed in matrix form by substituting (5) and (7) into (9), as follows:

$$\begin{bmatrix}\Delta\omega_{\mathrm{m}}\\ 0\end{bmatrix} = \boldsymbol{Z}_{\omega\mathrm{m}1}\Delta\boldsymbol{i}_{\mathrm{s}}^{\mathrm{s}} + \boldsymbol{Z}_{\omega\mathrm{m}2}\Delta\boldsymbol{i}_{\mathrm{r}}^{\mathrm{s}} \tag{10}$$

with

$$\begin{cases}\boldsymbol{Z}_{\omega\mathrm{m}1} = \begin{bmatrix}-I_{\mathrm{rq}}^{\mathrm{s}} & I_{\mathrm{rd}}^{\mathrm{s}}\\ 0 & 0\end{bmatrix}\cdot\\ \dfrac{3sp^2L_{\mathrm{m}}}{2\left(s^2J_{\mathrm{m}}+s\left(D_{\mathrm{m}}+D_{\mathrm{tm}}\left(1-pNH_{\mathrm{m}}\right)\right)+K_{\mathrm{tm}}\left(1-pNH_{\mathrm{m}}\right)\right)}\\ \boldsymbol{Z}_{\omega\mathrm{m}2} = \begin{bmatrix}I_{\mathrm{sq}}^{\mathrm{s}} & -I_{\mathrm{sd}}^{\mathrm{s}}\\ 0 & 0\end{bmatrix}\cdot\\ \dfrac{3sp^2L_{\mathrm{m}}}{2\left(s^2J_{\mathrm{m}}+s\left(D_{\mathrm{m}}+D_{\mathrm{tm}}\left(1-pNH_{\mathrm{m}}\right)\right)+K_{\mathrm{tm}}\left(1-pNH_{\mathrm{m}}\right)\right)}\end{cases} \tag{11}$$

where H_{m} is the transfer function from ω_{m} to Ω_{tur} given by

$$H_{\mathrm{m}} = \frac{2NK_{\mathrm{tm}}+2sND_{\mathrm{tm}}}{2pN^2\left(s^2J_{\mathrm{t}}+sD_{\mathrm{t}}+sD_{\mathrm{m}}+K_{\mathrm{tm}}\right)-sp\pi\rho r^4\left(c_1V_{\mathrm{w}}+2c_2r\Omega_{\mathrm{tur}}\right)}. \tag{12}$$

The angular frequency ω_{r} of rotor voltage and current is related to the rotor speed ω_{m} by $\omega_{\mathrm{r}} = \omega_{\mathrm{s}} - \omega_{\mathrm{m}}$. Considering a constant value for the system angular frequency ω_{s}, the corresponding small-signal model can be written as

$$\Delta\omega_{\mathrm{r}} = -\Delta\omega_{\mathrm{m}}. \tag{13}$$

Therefore, considering the small-signal characteristics of rotor speed, the linearized form of the stator voltage equation for the DFIG main circuit can be expressed as

$$\Delta\boldsymbol{u}_{\mathrm{s}}^{\mathrm{s}} = \boldsymbol{Z}_{\mathrm{ess}}\Delta\boldsymbol{i}_{\mathrm{s}}^{\mathrm{s}} + \boldsymbol{Z}_{\mathrm{esr}}\Delta\boldsymbol{i}_{\mathrm{r}}^{\mathrm{s}} \tag{14}$$

$$\boldsymbol{Z}_{\mathrm{ess}} = \begin{bmatrix}R_{\mathrm{s}}+sL_{\mathrm{s}} & -\omega_{\mathrm{s}}L_{\mathrm{s}}\\ \omega_{\mathrm{s}}L_{\mathrm{s}} & R_{\mathrm{s}}+sL_{\mathrm{s}}\end{bmatrix}$$

$$\boldsymbol{Z}_{\mathrm{esr}} = \begin{bmatrix}sL_{\mathrm{m}} & -\omega_{\mathrm{s}}L_{\mathrm{m}}\\ \omega_{\mathrm{s}}L_{\mathrm{m}} & sL_{\mathrm{m}}\end{bmatrix}. \tag{15}$$

Similarly, the linearized form of the rotor voltage equation is expressed as follows:

$$\Delta\boldsymbol{u}_{\mathrm{r}}^{\mathrm{s}} = \boldsymbol{Z}_{\mathrm{err}}\Delta\boldsymbol{i}_{\mathrm{r}}^{\mathrm{s}} + \boldsymbol{Z}_{\mathrm{ers}}\Delta\boldsymbol{i}_{\mathrm{s}}^{\mathrm{s}} + \boldsymbol{Z}_{\omega\mathrm{r}}\begin{bmatrix}\Delta\omega_{\mathrm{m}}\\ 0\end{bmatrix} \tag{16}$$

$$\boldsymbol{Z}_{\mathrm{err}} = \begin{bmatrix}R_{\mathrm{r}}+sL_{\mathrm{r}} & -\omega_{\mathrm{r}}L_{\mathrm{r}}\\ \omega_{\mathrm{r}}L_{\mathrm{r}} & R_{\mathrm{r}}+sL_{\mathrm{r}}\end{bmatrix}$$

$$\boldsymbol{Z}_{\mathrm{ers}} = \begin{bmatrix}sL_{\mathrm{m}} & -\omega_{\mathrm{r}}L_{\mathrm{m}}\\ \omega_{\mathrm{r}}L_{\mathrm{m}} & sL_{\mathrm{m}}\end{bmatrix}$$

$$\boldsymbol{Z}_{\omega\mathrm{r}} = \begin{bmatrix}L_{\mathrm{m}}I_{\mathrm{sq}}^{\mathrm{s}}+L_{\mathrm{r}}I_{\mathrm{rq}}^{\mathrm{s}} & 0\\ -L_{\mathrm{m}}I_{\mathrm{sd}}^{\mathrm{s}}-L_{\mathrm{r}}I_{\mathrm{rd}}^{\mathrm{s}} & 0\end{bmatrix} \tag{17}$$

where L_{s} and L_{r} are the stator and rotor inductances and R_{s} and R_{r} are the stator and rotor resistances, respectively.

B. Impedance Modeling of RSC Part

The power loop of RSC control receives power references dispatched by the WFC to regulate DFIG PCC power. The current loop controls the rotor current according to references generated by the power loop. Due to the presence of the decoupling term $\omega_{\mathrm{r}}\sigma L_{\mathrm{r}}$ in RSC control, the impedance model of the RSC part incorporates rotor speed dynamics. Where $\sigma = 1 - L_{\mathrm{m}}^2/L_{\mathrm{s}}L_{\mathrm{r}}$ is the leakage inductance coefficient. According to the control structure and considering the small-signal characteristics of rotor speed, the impedance model of RSC control can be written as

$$\Delta\boldsymbol{u}_{\mathrm{r}}^{\mathrm{c}} = \boldsymbol{Z}_{\mathrm{rsc,PQ}}\left(\begin{bmatrix}\Delta P_{\mathrm{t,ref}}\\ \Delta Q_{\mathrm{t,ref}}\end{bmatrix} - \begin{bmatrix}\Delta P_{\mathrm{t}}\\ \Delta Q_{\mathrm{t}}\end{bmatrix}\right) + \boldsymbol{Z}_{\mathrm{rsc,ir}}\Delta\boldsymbol{i}_{\mathrm{r}}^{\mathrm{c}} + \boldsymbol{Z}_{\mathrm{rsc},\omega}\begin{bmatrix}\Delta\omega_{\mathrm{m}}\\ 0\end{bmatrix} \tag{18}$$

$$\boldsymbol{Z}_{\mathrm{rsc,PQ}} = \begin{bmatrix}G_{\mathrm{pi,PQ}}G_{\mathrm{pi,ir}} & 0\\ 0 & -G_{\mathrm{pi,PQ}}G_{\mathrm{pi,ir}}\end{bmatrix}$$

$$\boldsymbol{Z}_{\mathrm{rsc,ir}} = \begin{bmatrix}-G_{\mathrm{pi,ir}} & -\omega_{\mathrm{r}}\sigma L_{\mathrm{r}}\\ \omega_{\mathrm{r}}\sigma L_{\mathrm{r}} & -G_{\mathrm{pi,ir}}\end{bmatrix}$$

$$\boldsymbol{Z}_{\mathrm{rsc},\omega} = \begin{bmatrix}\sigma L_{\mathrm{r}}I_{\mathrm{rq}}^{\mathrm{s}} & 0\\ -\sigma L_{\mathrm{r}}I_{\mathrm{rd}}^{\mathrm{s}} & 0\end{bmatrix} \tag{19}$$

where $G_{\mathrm{pi,PQ}} = k_{\mathrm{p,PQ}} + k_{\mathrm{i,PQ}}/s$ and $G_{\mathrm{pi,ir}} = k_{\mathrm{p,ir}} + k_{\mathrm{i,ir}}/s$ are the PI transfer functions of the RSC power and current loops, respectively.

The total active and reactive power at the DFIG PCC can be represented in the control system dq-frame, as follows:

$$\begin{aligned}P_{\mathrm{t}} &= -1.5(u_{\mathrm{sd}}^{\mathrm{c}}i_{\mathrm{td}}^{\mathrm{c}} + u_{\mathrm{sq}}^{\mathrm{c}}i_{\mathrm{tq}}^{\mathrm{c}})\\ Q_{\mathrm{t}} &= -1.5(u_{\mathrm{sq}}^{\mathrm{c}}i_{\mathrm{td}}^{\mathrm{c}} - u_{\mathrm{sd}}^{\mathrm{c}}i_{\mathrm{tq}}^{\mathrm{c}}).\end{aligned} \tag{20}$$

By linearizing (20), the small-signal model of DFIG output power can be derived as

$$\begin{bmatrix}\Delta P_{\mathrm{t}}\\ \Delta Q_{\mathrm{t}}\end{bmatrix} = \boldsymbol{G}_{\mathrm{it}}\Delta\boldsymbol{u}_{\mathrm{s}}^{\mathrm{c}} + \boldsymbol{G}_{\mathrm{us}}\Delta\boldsymbol{i}_{\mathrm{t}}^{\mathrm{c}} \tag{21}$$

$$\boldsymbol{G}_{\mathrm{it}} = -\begin{bmatrix}1.5I_{\mathrm{td}}^{\mathrm{s}} & 1.5I_{\mathrm{tq}}^{\mathrm{s}}\\ -1.5I_{\mathrm{tq}}^{\mathrm{s}} & 1.5I_{\mathrm{td}}^{\mathrm{s}}\end{bmatrix}$$

$$\boldsymbol{G}_{\mathrm{us}} = -\begin{bmatrix}1.5U_{\mathrm{sd}}^{\mathrm{s}} & 1.5U_{\mathrm{sq}}^{\mathrm{s}}\\ 1.5U_{\mathrm{sq}}^{\mathrm{s}} & -1.5U_{\mathrm{sd}}^{\mathrm{s}}\end{bmatrix}. \tag{22}$$

This section is dedicated to derive the DFIG impedance, with a temporary ignore for WFC dynamics. It is assumed that $[\Delta P_{\mathrm{t,ref}},\ \ \Delta Q_{\mathrm{t,ref}}]^{\mathrm{T}} = [0,\ \ 0]^{\mathrm{T}}$. Therefore, substituting (21) and (10) into (18) and transforming rotor voltage and current to the local grid dq-frame according to (1). Then, the impedance relation between stator voltage, stator current, and PCC total current in the RSC part is derived by combining (14) and (16) as

$$\boldsymbol{Z}_1\Delta\boldsymbol{u}_{\mathrm{s}}^{\mathrm{s}} = \boldsymbol{Z}_2\Delta\boldsymbol{i}_{\mathrm{s}}^{\mathrm{s}} + \boldsymbol{Z}_3\Delta\boldsymbol{i}_{\mathrm{t}}^{\mathrm{s}} \tag{23}$$

where the detailed expressions for $\boldsymbol{Z}_1$, $\boldsymbol{Z}_2$, and $\boldsymbol{Z}_3$ are presented in (24) shown at the bottom of the next page.

C. DFIG Impedance Synthesis

According to the DFIG structure shown in Fig. 2, the GSC and RSC are interconnected through the dc bus. Therefore, the dc voltage dynamics are influenced by both the power of the GSC and RSC, i.e., the voltage and current of the GSC and the rotor. The voltage loop of the GSC control regulates the dc voltage. Consequently, the dynamic characteristics of the dc voltage, in turn, affect the impedance modeling of the GSC part. Since the GSC control is not directly influenced by rotor speed dynamics, the impedance derivation of components within the GSC part remains consistent with existing studies, as detailed in Appendix A.

By referencing the impedance modeling of the RSC part, the impedance relation between stator voltage, stator current, and GSC current in the GSC part can be deduced as

$$\boldsymbol{Z}_4\Delta\boldsymbol{u}_{\mathrm{s}}^{\mathrm{s}} = \boldsymbol{Z}_5\Delta\boldsymbol{i}_{\mathrm{s}}^{\mathrm{s}} + \boldsymbol{Z}_6\Delta\boldsymbol{i}_{\mathrm{g}}^{\mathrm{s}} \tag{25}$$

where the detailed expressions for $\boldsymbol{Z}_4$, $\boldsymbol{Z}_5$, and $\boldsymbol{Z}_6$ as shown in (26) shown at the bottom of this page. $\boldsymbol{E}$ is a two-dimensional unit diagonal matrix. It is crucial to emphasize that when deriving the impedance relation for the GSC part, substituting (14) and (16) is necessary to eliminate rotor voltage and current perturbations introduced by dc voltage perturbations. However, this substitution will incorporate rotor speed perturbations. Therefore, rotor speed dynamics can indirectly impact the impedance characteristics of the GSC part through dc voltage.

Combining (23) and (25), and noting that $\Delta\boldsymbol{i}_{\mathrm{t}}^{\mathrm{s}} = \Delta\boldsymbol{i}_{\mathrm{s}}^{\mathrm{s}} - \Delta\boldsymbol{i}_{\mathrm{g}}^{\mathrm{s}}$, the full-frequency DFIG impedance $\boldsymbol{Z}_{\mathrm{dfig}}$ in the dq-frame, which characterizes the couplings between mechanical and electromagnetic dynamics, can be modeled as

$$\Delta\boldsymbol{u}_{\mathrm{s}}^{\mathrm{s}} = \boldsymbol{Z}_{\mathrm{dfig}}\Delta\boldsymbol{i}_{\mathrm{t}}^{\mathrm{s}} \tag{27}$$

with

$$\begin{aligned}\boldsymbol{Z}_{\mathrm{dfig}} = &-\left(\boldsymbol{Z}_4 - (\boldsymbol{Z}_5+\boldsymbol{Z}_6)\,\boldsymbol{Z}_2^{-1}\boldsymbol{Z}_1\right)^{-1}\\ &\times\left(\boldsymbol{Z}_6 + (\boldsymbol{Z}_5+\boldsymbol{Z}_6)\,\boldsymbol{Z}_2^{-1}\boldsymbol{Z}_3\right).\end{aligned} \tag{28}$$

According to the impedance derivation in this section, the transfer relationships for small-signal perturbations within the DFIG can be established, as depicted in Fig. 3. Note that including $[\Delta P_{\mathrm{t,ref}},\ \ \Delta Q_{\mathrm{t,ref}}]^{\mathrm{T}}$ as an input in the perturbation transfer relationships aims to ensure the applicability of Fig. 3, particularly when considering the WFC. The DFIG impedance modeled in this section represents a specific scenario where $[\Delta P_{\mathrm{t,ref}},\ \ \Delta Q_{\mathrm{t,ref}}]^{\mathrm{T}}$ is a zero vector. The direct propagation paths of rotor speed perturbations are highlighted in red. These perturbations enter the electrical subsystem, inducing responses in all system variables. Eventually, they influence the rotor speed through stator and rotor currents. This cyclic behavior of small-signal perturbations circulating between rotor speed and currents underscores the couplings between mechanical and electromagnetic dynamics. In addition, the transfer function between arbitrary perturbations as well as the dominant impedance blocks can be easily obtained according to Fig. 3, providing a reference for parameter optimization or impedance reshaping to improve DFIG stability.

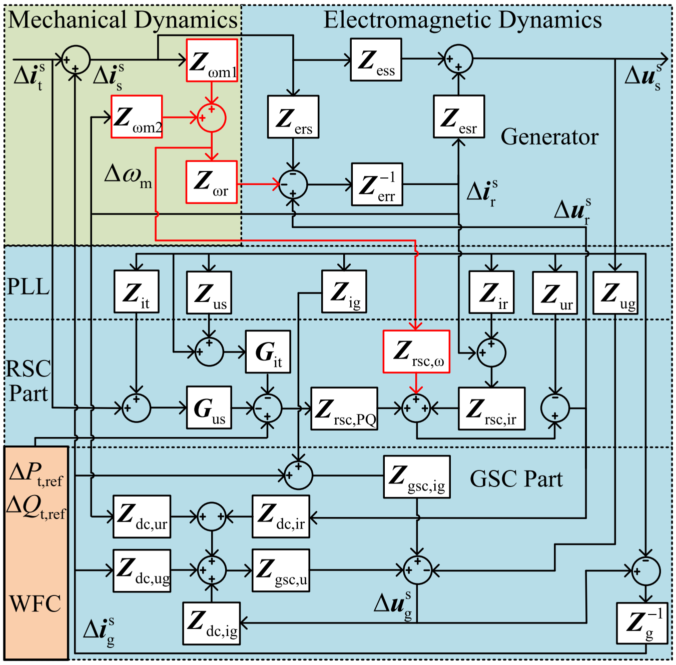

Fig. 3. Transfer relationships for small-signal perturbations within the DFIG.

III. Impedance Modeling of DFIG-Based Wind Farm Considering WFC Dynamics

A. *Systematic Analysis of WFC*

The configuration of WFC, as illustrated in Fig. 1, refers to the standard control system defined by Western Electricity Coordinating Council (WECC) [21]. This system comprises power control and power dispatch components, as depicted in Fig. 4. This article specifically focuses on analyzing the small-signal characteristics of power control within the WFC while ignoring the frequency and voltage subordinated control loops. The power control module receives power demand commands for the wind farm from the system operator. By combining these commands with output power measured at the wind farm PCC, PI regulations can determine the wind farm power references.

$$\begin{cases}\boldsymbol{Z}_1 = \boldsymbol{Z}_{\mathrm{ur}} + \boldsymbol{Z}_{\mathrm{rsc,PQ}}\left(\boldsymbol{G}_{\mathrm{it}} + \boldsymbol{G}_{\mathrm{it}}\boldsymbol{Z}_{\mathrm{us}} + \boldsymbol{G}_{\mathrm{us}}\boldsymbol{Z}_{\mathrm{it}}\right) - \boldsymbol{Z}_{\mathrm{rsc,ir}}\left(\boldsymbol{Z}_{\mathrm{esr}}^{-1} + \boldsymbol{Z}_{\mathrm{ir}}\right) + \left(\boldsymbol{Z}_{\mathrm{err}} + \left(\boldsymbol{Z}_{\omega\mathrm{r}} - \boldsymbol{Z}_{\mathrm{rsc},\omega}\right)\boldsymbol{Z}_{\omega\mathrm{m2}}\right)\boldsymbol{Z}_{\mathrm{esr}}^{-1}\\ \boldsymbol{Z}_2 = \boldsymbol{Z}_{\mathrm{rsc},\omega}\boldsymbol{Z}_{\omega\mathrm{m1}} - \boldsymbol{Z}_{\omega\mathrm{r}}\boldsymbol{Z}_{\omega\mathrm{m1}} - \boldsymbol{Z}_{\mathrm{ers}} + \left(\boldsymbol{Z}_{\mathrm{err}} - \boldsymbol{Z}_{\mathrm{rsc,ir}} - \boldsymbol{Z}_{\mathrm{rsc},\omega}\boldsymbol{Z}_{\omega\mathrm{m2}} + \boldsymbol{Z}_{\omega\mathrm{r}}\boldsymbol{Z}_{\omega\mathrm{m2}}\right)\boldsymbol{Z}_{\mathrm{esr}}^{-1}\boldsymbol{Z}_{\mathrm{ess}}\\ \boldsymbol{Z}_3 = -\boldsymbol{Z}_{\mathrm{rsc,PQ}}\boldsymbol{G}_{\mathrm{us}}.\end{cases} \tag{24}$$

$$\begin{cases}\boldsymbol{Z}_4 = \boldsymbol{E} + \boldsymbol{Z}_{\mathrm{ug}} - \boldsymbol{Z}_{\mathrm{gsc,u}}\boldsymbol{Z}_{\mathrm{dc,ig}} - \boldsymbol{Z}_{\mathrm{gsc,u}}\boldsymbol{Z}_{\mathrm{dc,ur}}\boldsymbol{Z}_{\mathrm{esr}}^{-1} - \boldsymbol{Z}_{\mathrm{gsc,ig}}\boldsymbol{Z}_{\mathrm{ig}} - \boldsymbol{Z}_{\mathrm{gsc,u}}\boldsymbol{Z}_{\mathrm{dc,ir}}\left(\boldsymbol{Z}_{\mathrm{err}} + \boldsymbol{Z}_{\omega\mathrm{r}}\boldsymbol{Z}_{\omega\mathrm{m2}}\right)\boldsymbol{Z}_{\mathrm{esr}}^{-1}\\ \boldsymbol{Z}_5 = \boldsymbol{Z}_{\mathrm{gsc,u}}\boldsymbol{Z}_{\mathrm{dc,ir}}\left(\boldsymbol{Z}_{\mathrm{ers}} - \boldsymbol{Z}_{\mathrm{err}}\boldsymbol{Z}_{\mathrm{esr}}^{-1}\boldsymbol{Z}_{\mathrm{ess}} + \boldsymbol{Z}_{\omega\mathrm{r}}\boldsymbol{Z}_{\omega\mathrm{m1}} - \boldsymbol{Z}_{\omega\mathrm{r}}\boldsymbol{Z}_{\omega\mathrm{m2}}\boldsymbol{Z}_{\mathrm{esr}}^{-1}\boldsymbol{Z}_{\mathrm{ess}}\right) - \boldsymbol{Z}_{\mathrm{gsc,u}}\boldsymbol{Z}_{\mathrm{dc,ur}}\boldsymbol{Z}_{\mathrm{esr}}^{-1}\boldsymbol{Z}_{\mathrm{ess}}\\ \boldsymbol{Z}_6 = \boldsymbol{Z}_{\mathrm{gsc,u}}\boldsymbol{Z}_{\mathrm{dc,ig}}\boldsymbol{Z}_{\mathrm{g}} + \boldsymbol{Z}_{\mathrm{gsc,u}}\boldsymbol{Z}_{\mathrm{dc,ug}} + \boldsymbol{Z}_{\mathrm{gsc,ig}} - \boldsymbol{Z}_{\mathrm{g}}.\end{cases} \tag{26}$$

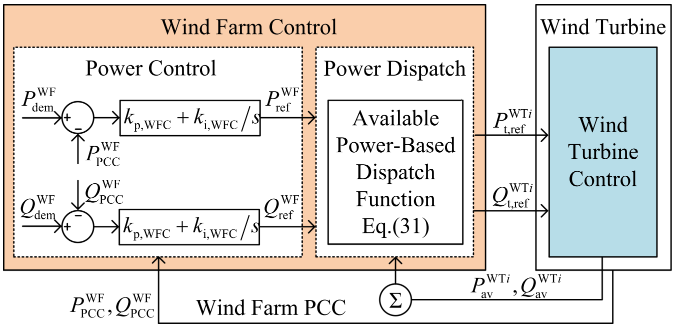

Fig. 4. Structure diagram of the WFC.

Subsequently, the power dispatch module converts these wind farm power references into WT power references for each DFIG in a specific ratio. This ratio is determined by the dispatch function, designed with flexible options, such as average dispatch or proportional dispatch based on WT installed capacities [22]. This article adopts the prevalent available power-based dispatch function, fully considering the generation capacities of each DFIG [5].

For a wind farm containing a total of n DFIGs, the available active power $P_{\text{av}}^{\text{WT}i}$ of the ith DFIG at the current wind speed V_{w} is given by

$$P_{\text{av}}^{\text{WT}i}=\frac{1}{2}\pi\rho r^2V_{\text{w}}^3C_{\text{p\_max}}. \tag{29}$$

When employing fixed pitch angle control with $\beta=0$, the maximum rotor power coefficient $C_{\text{p\_max}}$ is 0.44. It is essential to emphasize that the available power must be constrained within the rated power of the DFIG. Therefore, the corresponding available reactive power $Q_{\text{av}}^{\text{WT}i}$ for the ith DFIG can be calculated as

$$Q_{\text{av}}^{\text{WT}i}=\sqrt{\left(S_{\text{rated}}^{\text{WT}i}\right)^2-\left(P_{\text{av}}^{\text{WT}i}\right)^2} \tag{30}$$

where $S_{\text{rated}}^{\text{WT}i}$ is the rated apparent power of the ith DFIG.

Consequently, the active and reactive power references for the ith DFIG can be determined according to the available power-based dispatch function as follows:

$$P_{\text{t,ref}}^{\text{WT}i}=\frac{P_{\text{av}}^{\text{WT}i}}{\sum_{i=1}^{n}P_{\text{av}}^{\text{WT}i}}P_{\text{ref}}^{\text{WF}},\quad Q_{\text{t,ref}}^{\text{WT}i}=\frac{Q_{\text{av}}^{\text{WT}i}}{\sum_{i=1}^{n}Q_{\text{av}}^{\text{WT}i}}Q_{\text{ref}}^{\text{WF}}. \tag{31}$$

Similarly, it is crucial to ensure that the power references for each DFIG do not exceed its rated power. The coefficients for dispatching active and reactive power for the ith DFIG, denoted as $r_{\text{P}i}$ and $r_{\text{Q}i}$, respectively, can be defined as

$$r_{\text{P}i}=\frac{P_{\text{av}}^{\text{WT}i}}{\sum_{i=1}^{n}P_{\text{av}}^{\text{WT}i}},\quad r_{\text{Q}i}=\frac{Q_{\text{av}}^{\text{WT}i}}{\sum_{i=1}^{n}Q_{\text{av}}^{\text{WT}i}}. \tag{32}$$

B. Remodeling of DFIG Impedance Considering WFC Dynamics

According to the WFC structure, small-signal perturbations occurring within the wind farm can propagate to the WFC through the measured power at the wind farm PCC. This propagation leads to corresponding variations in the power references within the power control module. Eventually, these power reference perturbations are transmitted to each DFIG through the power dispatch module. Therefore, it can be concluded that the WFC dynamics impact the small-signal characteristics of the DFIG. In this section, the DFIG impedance is remodeled to consider the small-signal characteristics of the WFC, aiming to capture the couplings between the WFC and the DFIG.

The small-signal model for the power control module of the WFC can be formulated as

$$\begin{bmatrix}\Delta P_{\text{ref}}^{\text{WF}}\\ \Delta Q_{\text{ref}}^{\text{WF}}\end{bmatrix}=\boldsymbol{Z}_{\text{WFC}}\begin{bmatrix}\Delta P_{\text{pcc}}^{\text{WF}}\\ \Delta Q_{\text{pcc}}^{\text{WF}}\end{bmatrix} \tag{33}$$

$$\boldsymbol{Z}_{\text{WFC}}=\begin{bmatrix}-G_{\text{pi,WFC}} & 0\\ 0 & -G_{\text{pi,WFC}}\end{bmatrix} \tag{34}$$

where $G_{\text{pi,WFC}}=k_{\text{p,WFC}}+k_{\text{i,WFC}}/s$ represents the PI transfer function for power control in the WFC.

The small-signal characteristics of wind farm PCC power can refer to (20) and (21). Therefore, the linearization model for wind farm PCC power is directly given by

$$\begin{bmatrix}\Delta P_{\text{pcc}}^{\text{WF}}\\ \Delta Q_{\text{pcc}}^{\text{WF}}\end{bmatrix}=\boldsymbol{G}_{\text{ipcc}}\Delta\boldsymbol{u}_{\text{pcc}}^{\text{c}}+\boldsymbol{G}_{\text{upcc}}\Delta\boldsymbol{i}_{\text{pcc}}^{\text{c}} \tag{35}$$

$$\boldsymbol{G}_{\text{ipcc}}=\begin{bmatrix}1.5I_{\text{pccd}}^{\text{g}} & 1.5I_{\text{pccq}}^{\text{g}}\\ -1.5I_{\text{pccq}}^{\text{g}} & 1.5I_{\text{pccd}}^{\text{g}}\end{bmatrix}$$

$$\boldsymbol{G}_{\text{upcc}}=\begin{bmatrix}1.5U_{\text{pccd}}^{\text{g}} & 1.5U_{\text{pccq}}^{\text{g}}\\ 1.5U_{\text{pccq}}^{\text{g}} & -1.5U_{\text{pccd}}^{\text{g}}\end{bmatrix} \tag{36}$$

where $\boldsymbol{u}_{\text{pcc}}$ and $\boldsymbol{i}_{\text{pcc}}$ are the voltage and current at the wind farm PCC. The superscript “g” indicates variables in the global grid dq-frame defined by the wind farm PCC voltage.

It should be noted that the d-axis and q-axis components of the voltage and current perturbations in (35) are in the WFC system dq-frame. This dq-frame is defined by the PLL in the WFC when measuring wind farm PCC power in the dq-frame. Therefore, direct utilization of (1) for transforming variables to the global grid dq-frame is not feasible. Considering the PLL structure, it is necessary to replace Z_{pll} with $Z_{\text{pll}}^{\text{WF}}$

$$Z_{\text{pll}}^{\text{WF}}=\frac{sk_{\text{ppll}}^{\text{WF}}+k_{\text{ipll}}^{\text{WF}}}{s^2+sU_{\text{pccd}}^{\text{g}}k_{\text{ppll}}^{\text{WF}}+U_{\text{pccd}}^{\text{g}}k_{\text{ipll}}^{\text{WF}}} \tag{37}$$

where $k_{\text{ppll}}^{\text{WF}}$ and $k_{\text{ipll}}^{\text{WF}}$ are the PI parameters of the PLL in the WFC. Consequently, the coordinate transformation relation for small-signal perturbations within the WFC is rewritten as

$$\Delta\boldsymbol{x}^{\text{c}}=\boldsymbol{Z}_{\text{x}}^{\text{WF}}\Delta\boldsymbol{u}_{\text{pcc}}^{\text{g}}+\Delta\boldsymbol{x}^{\text{g}} \tag{38}$$

$$\boldsymbol{Z}_{\text{x}}^{\text{WF}}=\begin{bmatrix}0 & Z_{\text{pll}}^{\text{WF}}X_{\text{q}}^{\text{g}}\\ 0 & -Z_{\text{pll}}^{\text{WF}}X_{\text{d}}^{\text{g}}\end{bmatrix}. \tag{39}$$

The measurement of wind farm PCC power can also be realized in the abc-frame or $\alpha\beta$-frame without requiring a PLL. The WFC system dq-frame aligns with the global grid dq-frame.

In this scenario, (38) is still applicable for the generality of impedance modeling, except that $\boldsymbol{Z}_{\text{x}}^{\text{WF}}$ needs to be defined as a zero matrix.

When analyzing the impedance characteristics of the wind farm, transient changes in wind speed are disregarded, and a constant wind speed is assumed. Consequently, the power dispatch coefficients $r_{\text{P}i}$ and $r_{\text{Q}i}$ in the power dispatch module for each DFIG are considered as constant coefficients. By combining (33), (35), and (38), the small-signal model of the power references for an individual DFIG within the wind farm can be derived as

$$\begin{bmatrix}\Delta P_{\text{t,ref}}^{\text{WT}i}\\ \Delta Q_{\text{t,ref}}^{\text{WT}i}\end{bmatrix} = \boldsymbol{Z}_{\text{r}i}\boldsymbol{Z}_{\text{WFC}}\boldsymbol{G}_{\text{upcc}}\Delta\boldsymbol{i}_{\text{pcc}}^{\text{g}} + \boldsymbol{Z}_{\text{r}i}\boldsymbol{Z}_{\text{WFC}} \times \left(\boldsymbol{G}_{\text{ipcc}} + \boldsymbol{G}_{\text{ipcc}}\boldsymbol{Z}_{\text{upcc}}^{\text{WF}} + \boldsymbol{G}_{\text{upcc}}\boldsymbol{Z}_{\text{ipcc}}^{\text{WF}}\right)\Delta\boldsymbol{u}_{\text{pcc}}^{\text{g}} \tag{40}$$

where

$$\boldsymbol{Z}_{\text{r}i} = \begin{bmatrix} r_{\text{P}i} & 0\\ 0 & r_{\text{Q}i}\end{bmatrix}. \tag{41}$$

The power reference perturbations in (40) will influence the DFIG impedance through RSC control. Therefore, the $[\Delta P_{\text{t,ref}},\ \ \Delta Q_{\text{t,ref}}]^{\text{T}}$ in (18) is no longer a zero vector. Substituting (40) into (18) modifies the impedance relationship of the RSC part, considering the typical millisecond-scale communication time delay T_{d} in WFC signals [23]. Importantly, this modification preserves the original impedances $\boldsymbol{Z}_1$, $\boldsymbol{Z}_2$, and $\boldsymbol{Z}_3$. Equation (23) can be rewritten as

$$\boldsymbol{Z}_1\Delta\boldsymbol{u}_{\text{s}}^{\text{s}} = \boldsymbol{Z}_2\Delta\boldsymbol{i}_{\text{s}}^{\text{s}} + \boldsymbol{Z}_3\Delta\boldsymbol{i}_{\text{t}}^{\text{s}} + \boldsymbol{Z}_7\Delta\boldsymbol{u}_{\text{pcc}}^{\text{g}} + \boldsymbol{Z}_8\Delta\boldsymbol{i}_{\text{pcc}}^{\text{g}} \tag{42}$$

with

$$\begin{cases}\boldsymbol{Z}_7 = \boldsymbol{Z}_{\text{rsc,PQ}}\boldsymbol{G}_{\text{d}}\boldsymbol{Z}_{\text{r}i}\boldsymbol{Z}_{\text{WFC}}(\boldsymbol{G}_{\text{ipcc}} + \boldsymbol{G}_{\text{ipcc}}\boldsymbol{Z}_{\text{upcc}}^{\text{WF}}\\ \qquad + \boldsymbol{G}_{\text{upcc}}\boldsymbol{Z}_{\text{ipcc}}^{\text{WF}})\\ \boldsymbol{Z}_8 = \boldsymbol{Z}_{\text{rsc,PQ}}\boldsymbol{G}_{\text{d}}\boldsymbol{Z}_{\text{r}i}\boldsymbol{Z}_{\text{WFC}}\boldsymbol{G}_{\text{upcc}}\end{cases}$$

$$\boldsymbol{G}_{\text{d}} = \begin{bmatrix}\dfrac{1-0.5T_{\text{d}}s}{1+0.5T_{\text{d}}s} & 0\\ 0 & \dfrac{1-0.5T_{\text{d}}s}{1+0.5T_{\text{d}}s}\end{bmatrix}. \tag{43}$$

The impedance relation (25) of the GSC part remains unchanged. Therefore, the DFIG impedance in the dq-frame, taking into account the small-signal characteristics of the WFC, is remodeled as

$$\Delta\boldsymbol{i}_{\text{t}}^{\text{s}} = \boldsymbol{Y}_{\text{dfig}}\Delta\boldsymbol{u}_{\text{s}}^{\text{s}} + \boldsymbol{Y}_{\text{vccs}}\Delta\boldsymbol{u}_{\text{pcc}}^{\text{g}} + \boldsymbol{Y}_{\text{cccs}}\Delta\boldsymbol{i}_{\text{pcc}}^{\text{g}} \tag{44}$$

with

$$\begin{cases}\boldsymbol{Y}_{\text{dfig}} = \boldsymbol{Z}_{\text{dfig}}^{-1}\\ \boldsymbol{Y}_{\text{vccs}} = -\left(\boldsymbol{Z}_6 + (\boldsymbol{Z}_5+\boldsymbol{Z}_6)\,\boldsymbol{Z}_2^{-1}\boldsymbol{Z}_3\right)^{-1}(\boldsymbol{Z}_5+\boldsymbol{Z}_6)\,\boldsymbol{Z}_2^{-1}\boldsymbol{Z}_7\\ \boldsymbol{Y}_{\text{cccs}} = -\left(\boldsymbol{Z}_6 + (\boldsymbol{Z}_5+\boldsymbol{Z}_6)\,\boldsymbol{Z}_2^{-1}\boldsymbol{Z}_3\right)^{-1}(\boldsymbol{Z}_5+\boldsymbol{Z}_6)\,\boldsymbol{Z}_2^{-1}\boldsymbol{Z}_8.\end{cases} \tag{45}$$

Comparing the equation above with the original DFIG impedance (27), it can be observed that the DFIG impedance with the small-signal characteristics of the WFC incorporates two additional terms associated with the small-signal perturbations of the wind farm PCC voltage and current. According to Kirchhoff's current law, these two components can be regarded as a current source controlled by the voltage and current perturbations at the wind farm PCC. Therefore, the DFIG impedance model, considering WFC dynamics, can be represented as shown in Fig. 5. In this representation, the dynamic couplings between the WFC and the DFIG are reflected by the controlled current source connected in parallel to the original impedance $\boldsymbol{Z}_{\text{dfig}}$. Furthermore, it is worth noting that the wind farm PCC voltage and current are influenced by the internal structures of the wind farm, including each DFIG and collector line. Therefore, this controlled current source also captures the dynamic couplings among DFIGs and between them and collector lines induced through the WFC.

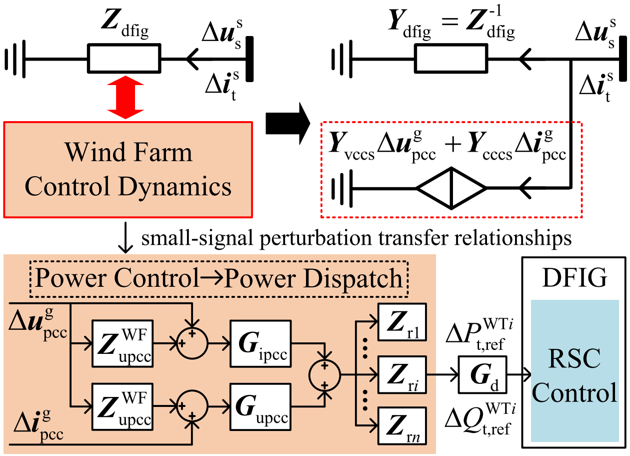

Fig. 5. DFIG impedance model with visualization of couplings introduced by WFC dynamics.

C. Impedance Modeling of DFIG-Based Wind Farm

This section develops the CIM for the wind farm equipped with the WFC, as depicted in Fig. 1. The wind farm consists of 10 feeders, each accommodating multiple DFIGs. It is assumed that a total of n DFIGs are distributed within the wind farm. Each DFIG is connected to the collector line via a $0.69/35$ kV transformer. All feeders are converged at the 35 kV bus, and their combined power is transmitted to the wind farm PCC through a transmission line. Finally, the power is delivered to the grid through a $35/220$ kV main transformer.

The grid-connected wind farm system operates at multiple voltage levels due to the presence of transformers. To facilitate impedance derivation for the wind farm, this article adopts the rated voltage of 35 kV for the collector line as the reference voltage. Consequently, it is necessary to convert the DFIG impedance to match the 35 kV voltage level. Furthermore, as mentioned in Section II, the DFIG impedance (44) is in the local grid dq-frame determined by its own PCC voltage. DFIGs with different PCC voltages have distinct local grid dq-frame. The impedance of these DFIGs cannot be directly connected to form an impedance network. Therefore, besides the voltage level conversion, it is also necessary to transform the DFIG impedance

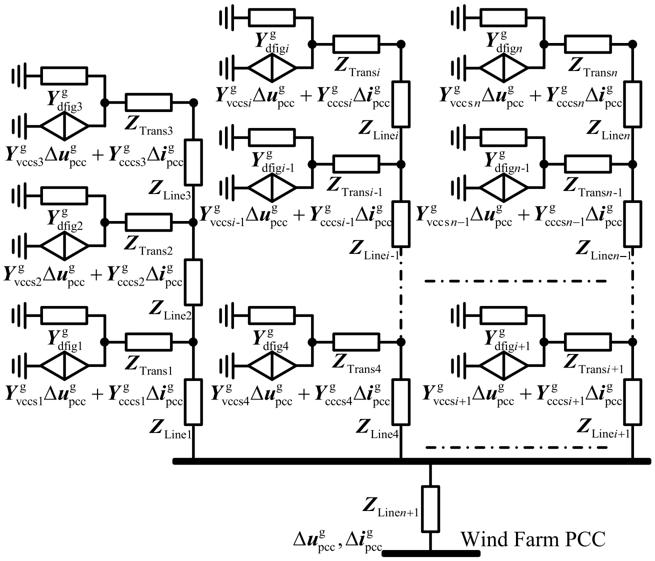

Fig. 6. Impedance network model of the wind farm in the global grid dq-frame considering multiple dynamic couplings.

into the global grid dq-frame defined by the wind farm PCC voltage [24].

The turn ratio of the DFIG transformer is $k_{\mathrm{T}} = 35/0.69$. The phase angle difference θ between the DFIG PCC voltage and the wind farm PCC voltage can be found based on the steady-state power flow calculation [25]. Finally, the discounted DFIG impedance in the global grid dq-frame is given by

$$\Delta \boldsymbol{i}_{\mathrm{t}}^{\mathrm{g}} = \boldsymbol{Y}_{\mathrm{dfig}}^{\mathrm{g}} \Delta \boldsymbol{u}_{\mathrm{s}}^{\mathrm{g}} + \boldsymbol{Y}_{\mathrm{vccs}}^{\mathrm{g}} \Delta \boldsymbol{u}_{\mathrm{pcc}}^{\mathrm{g}} + \boldsymbol{Y}_{\mathrm{cccs}}^{\mathrm{g}} \Delta \boldsymbol{i}_{\mathrm{pcc}}^{\mathrm{g}} \tag{46}$$

with

$$\begin{cases} \boldsymbol{Y}_{\mathrm{dfig}}^{\mathrm{g}} = \dfrac{\boldsymbol{T}_{\mathrm{dq}}^{-1} \boldsymbol{Y}_{\mathrm{dfig}} \boldsymbol{T}_{\mathrm{dq}}}{k_{\mathrm{T}}^{2}} \\ \boldsymbol{Y}_{\mathrm{vccs}}^{\mathrm{g}} = \dfrac{\boldsymbol{T}_{\mathrm{dq}}^{-1} \boldsymbol{Y}_{\mathrm{vccs}}}{k_{\mathrm{T}}} \\ \boldsymbol{Y}_{\mathrm{cccs}}^{\mathrm{g}} = \dfrac{\boldsymbol{T}_{\mathrm{dq}}^{-1} \boldsymbol{Y}_{\mathrm{cccs}}}{k_{\mathrm{T}}} \end{cases}$$

$$\boldsymbol{T}_{\mathrm{dq}} = \begin{bmatrix} \cos(\theta) & \sin(\theta) \\ -\sin(\theta) & \cos(\theta) \end{bmatrix}. \tag{47}$$

Based on investigations of several wind farms in a region of China, the maximum length of collector lines between neighboring WTs within a wind farm generally does not exceed 1 km. Moreover, the impact of parallel conductance in the collector lines on system stability is negligible and can be safely disregarded. Therefore, it is appropriate to use a lumped-element RL equivalent circuit to describe the collector line. The impedance for both the collector line and transformer in the global grid dq-frame can be expressed as

$$\boldsymbol{Z}_{\mathrm{Line/Trans}} = \begin{bmatrix} R + sL & -\omega_{\mathrm{s}} L \\ \omega_{\mathrm{s}} L & R + sL \end{bmatrix}. \tag{48}$$

Subsequently, the impedance network model in the global grid dq-frame can be established based on the wind farm topology, as shown in Fig. 6. The impedance of the ith DFIG, along with its connected transformer and collector line, is denoted by the subscript "i." However, due to the inclusion of current sources controlled by voltage and current perturbations at the wind farm PCC in the DFIG impedance model, the wind farm impedance cannot be directly aggregated through impedance series/parallel connections.

Referring to Fig. 6, the wind farm comprises a total of $2n + 2$ nodes, including the 35 kV bus and the wind farm PCC. Therefore, the node voltage equation for the wind farm impedance network can be formulated as

$$\boldsymbol{Y}_{\mathrm{IN}} \boldsymbol{U} = \boldsymbol{Y}_{\mathrm{INu}} \boldsymbol{U} + \boldsymbol{Y}_{\mathrm{INi}} \Delta \boldsymbol{i}_{\mathrm{pcc}}^{\mathrm{g}} \tag{49}$$

where $\boldsymbol{U} = [\Delta \boldsymbol{u}_{\mathrm{s}1}^{\mathrm{g}}, \ \ldots, \ \Delta \boldsymbol{u}_{\mathrm{s}n}^{\mathrm{g}}, \ \Delta \boldsymbol{u}_{\mathrm{pcc}}^{\mathrm{g}}]^{\mathrm{T}}$ is the node voltage vector. The right side of the equation is a summation of injected current sources at each node. For the DFIG node, the injected current source is controlled by the small-signal perturbations of the wind farm PCC voltage and current. Meanwhile, for the wind farm PCC node, the influence of the grid on this node is regarded as an injected current source with a value of $-\Delta \boldsymbol{i}_{\mathrm{pcc}}^{\mathrm{g}}$.

$\boldsymbol{Y}_{\mathrm{IN}}$ represents the node admittance matrix, primarily comprising DFIG impedance and collector line impedance. This matrix has dimensions of $4n + 4$, consisting of individual 2×2 admittance matrix cells within a $(2n + 2) \times (2n + 2)$ matrix. $\boldsymbol{Y}_{\mathrm{INu}}$ and $\boldsymbol{Y}_{\mathrm{INi}}$ represent the coefficient matrices for the voltage and current control variables of the controlled current source, respectively. $\boldsymbol{Y}_{\mathrm{INu}}$ is a $(4n + 4) \times (4n + 4)$ matrix, while $\boldsymbol{Y}_{\mathrm{INi}}$ is a $(4n + 4) \times 2$ matrix. It is worth mentioning that during the construction of the node voltage equation, the voltage control variable of the controlled current source on the right side of (49) should be $\Delta \boldsymbol{u}_{\mathrm{pcc}}^{\mathrm{g}}$. However, this voltage control variable is replaced with $\boldsymbol{U}$ for the convenience of subsequent wind farm impedance derivation. This modification alters the dimension of $\boldsymbol{Y}_{\mathrm{INu}}$, while the elements corresponding to $\Delta \boldsymbol{u}_{\mathrm{pcc}}^{\mathrm{g}}$ remain unchanged.

Reposition the voltage control current source from the right side of (49) to the left side. The wind farm impedance can be derived through inverse matrix calculation. Assuming the node order of the wind farm PCC is denoted as k, the CIM of the wind farm in the dq-frame is a 2×2 matrix consisting of all the elements of rows $2k - 1$ and $2k$ of $(\boldsymbol{Y}_{\mathrm{IN}} - \boldsymbol{Y}_{\mathrm{INu}})^{-1} \boldsymbol{Y}_{\mathrm{INi}}$, which can be formally expressed as

$$\boldsymbol{Z}_{\mathrm{windfarm}} = \left[(\boldsymbol{Y}_{\mathrm{IN}} - \boldsymbol{Y}_{\mathrm{INu}})^{-1} \boldsymbol{Y}_{\mathrm{INi}} \right]_{2k-1:2k,:} \tag{50}$$

IV. CHARACTERISTIC ANALYSIS OF CIM FOR DFIG-BASED WIND FARM

In this section, the frequency characteristics of the proposed CIM will be analyzed at both the DFIG and wind farm levels, respectively, compared with existing simplified impedance models. At the DFIG level, the influence of mechanical dynamics on impedance characteristics is mainly analyzed. At the wind farm level, the emphasis is placed on investigating the small-signal characteristics of the WFC and the impact of different WFC PI parameters on the wind farm impedance.

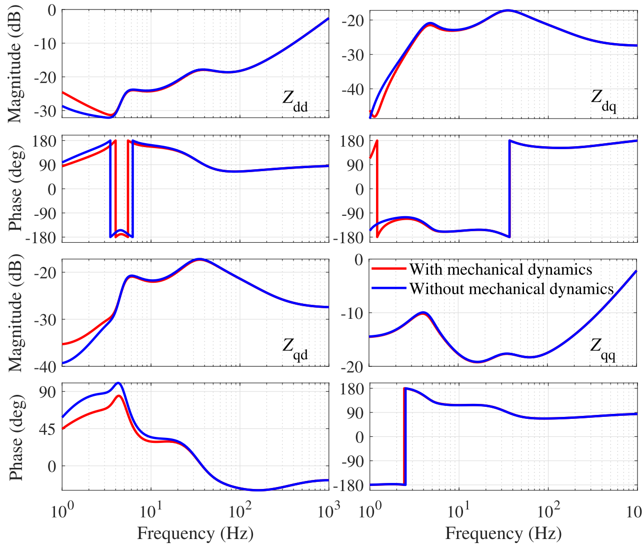

Fig. 7. Comparison results of the DFIG impedance with and without mechanical dynamics.

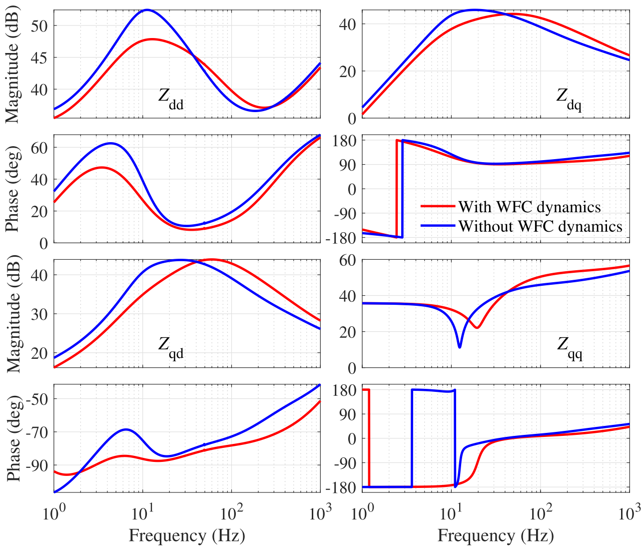

Fig. 8. Comparison results of CIM and simplified impedance for the wind farm.

A. Influence of Mechanical Dynamics on DFIG Impedance Characteristics

When analyzing the DFIG impedance characteristics, the small-signal characteristics of the WFC are currently not taken into consideration. Therefore, it can be assumed that the single DFIG depicted in Fig. 2 is directly connected to the grid. Thus, the full-frequency impedance model $\boldsymbol{Z}_{\rm dfig}$ for the DFIG derived in Section II is directly adopted. The basic parameters of the DFIG are presented in Table I in Appendix B. The wind speed is 12 m/s. The output active and reactive power of the DFIG are 2.5 MW and 0 MVar, respectively.

The results comparing the DFIG impedance derived in this article with the existing simplified impedance, which neglects mechanical dynamics, are presented in Fig. 7. It can be observed that the two impedance models exhibit almost identical behavior above 10 Hz in the dq-frame, while a significant difference exists between them in the frequency range below 10 Hz. This discrepancy can be attributed to the relatively slow time scale of mechanical dynamics, which plays a predominant role in shaping the low-frequency characteristics of DFIG impedance. In addition, the small difference in the $q-q$ channel impedance $Z_{\rm qq}$ over the full-frequency range can be explained by the fact that the effective quantity of the rotor speed perturbation $[\Delta\omega_{\rm m},\quad 0]^{\rm T}$ appears only at d-axis-related positions when deriving the DFIG impedance. Thus, mechanical dynamics have little effect on $Z_{\rm qq}$.

The consideration of mechanical dynamics yields distinct low-frequency characteristics of the DFIG impedance in the dq-frame, influencing stability analysis results within this frequency range. Reflecting this fact into the time domain of the stationary frame would manifest itself in the conclusion that neglecting mechanical dynamics can result in erroneous analyses of low-frequency power oscillations in grid-connected DFIG systems. Therefore, incorporating mechanical dynamics into the DFIG impedance is necessary to enhance its accuracy within the low-frequency band and to precisely analyze the low-frequency power oscillations caused by various factors, including mechanical dynamics.

B. Influence of WFC Dynamics on Wind Farm Impedance Characteristics

In order to simplify the analysis while maintaining generality, the wind farm depicted in Fig. 1 is represented by 10 DFIGs, each connected to the 35 kV bus through a 0.69/35 kV transformer and collector line. Power collected at the 35 kV bus is transmitted to the wind farm PCC through a transmission line. The basic parameters of the wind farm can be found in Tables I and II in Appendix B. The WFC PI parameters are $k_{\rm p,WFC}=0.3$ and $k_{\rm i,WFC}=3$. The demand commands for active and reactive power at the wind farm PCC are 20 MW and 0 MVar. The specific wind speed values for DFIGs can alter the steady-state operating point of the wind farm [26]. However, this does not affect the validity and applicability of the modeling and analysis methodology proposed for the wind farm CIM in this article. Considering the close proximity and similar wind conditions of the WTs within the same wind farm, the wind speeds of the 10 DFIGs are taken as 12 m/s, 11 m/s, 12 m/s, 11 m/s, 10 m/s, 10 m/s, 11 m/s, 12 m/s, 12 m/s, 12 m/s, respectively.

In accordance with the impedance modeling methodology introduced in Section III, the CIM for the wind farm considering the WFC dynamics is derived. It is subsequently compared with the simplified wind farm impedance, which is aggregated through series-parallel connections of DFIG impedance presented in Section II. The results are shown in Fig. 8. The figure clearly demonstrates that the WFC dynamics significantly influence wind farm impedance characteristics in the full-frequency range. This phenomenon arises because the impact of the WFC on DFIG impedance is represented by an additional current source controlled by the voltage and current perturbations at the wind farm PCC, which directly contributes to the derivation

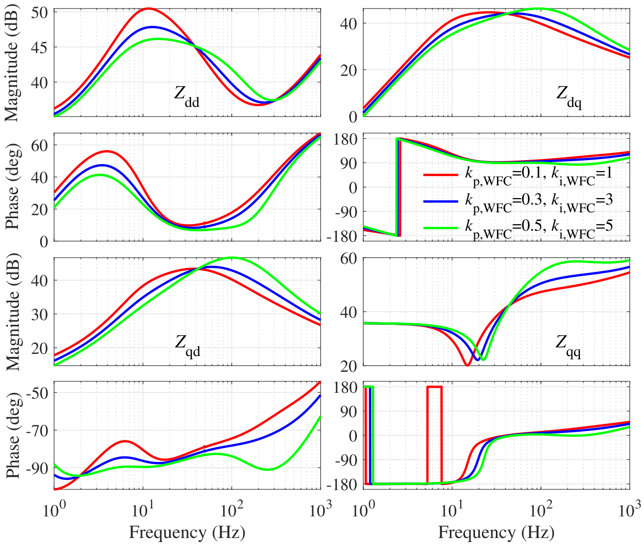

Fig. 9. Comparison results of wind farm impedance with different WFC PI parameters.

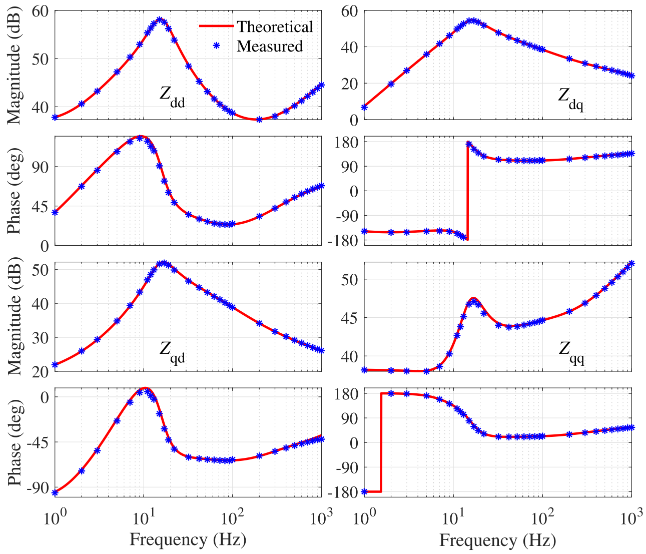

Fig. 10. Comparison results of theoretical CIM and frequency scanning measurements for the wind farm impedance.

process of wind farm impedance. Moreover, both voltage and current at the wind farm PCC depend on all electrical equipment within the wind farm. Consequently, the WFC enhances couplings not only among DFIGs but also between DFIGs and collector lines, further leading to a full-frequency variation of the wind farm impedance.

C. Influence of WFC PI Parameters on Wind Farm Impedance Characteristics

The derivation process of the wind farm CIM reveals that the impedance $\boldsymbol{Z}_{\mathrm{WFC}}$, reflecting the impact of WFC PI parameters, is propagated into the DFIG impedance and subsequently into the wind farm impedance. Therefore, this section provides a detailed analysis of the influence of WFC PI parameters on the wind farm impedance characteristics. The power control PI parameters of the WFC are adjusted while keeping the basic parameters and power demand commands of the wind farm unchanged. Fig. 9 illustrates that an increase in the PI parameters results in a wider frequency range in which both the $q-d$ channel impedance Z_{qd} and the $q-q$ channel impedance Z_{qq} of the wind farm CIM exhibit a negative resistive characteristic. This observation implies that excessively large WFC PI parameters enhance the susceptibility of the grid-connected wind farm system to instability [27].

V. SIMULATION AND CASE STUDIES

In this section, the accuracy of the proposed wind farm CIM will be verified through the frequency scanning method [28]. The performance of the CIM in stability analysis of the grid-connected wind farm system will be investigated using the generalized Nyquist criterion (GNC). Furthermore, the influence of the WFC PI parameters on system stability will be experimentally confirmed. These case studies are based on a simulation model of the 10 DFIGs wind farm developed in MATLAB/Simulink. The basic parameters of the wind farm refer to Tables I and II. The wind speeds for these 10 DFIGs are set at 12 m/s, 11 m/s, 12 m/s, 11 m/s, 10 m/s, 10 m/s, 11 m/s, 12 m/s, 12 m/s, 12 m/s.

A. Frequency Scanning Verification of Wind Farm CIM

Frequency scanning measurements of the wind farm impedance are conducted in MATLAB/Simulink. Voltage perturbations are injected with a harmonic frequency ranging from 1 Hz to 1000 Hz. The magnitude of the perturbations is set at 0.02 pu, which is sufficiently small to maintain system stability yet large enough for accurate identification of system impedance. By measuring the voltage and current responses at the wind farm PCC, wind farm impedance values corresponding to each perturbation frequency can be calculated. Fig. 10 illustrates the comparison between frequency scanning measurements and theoretically derived CIM when wind farm output active and reactive power are set at 15 MW and 0 MVar, respectively. The two exhibit excellent agreement, validating the wind farm CIM. At the same time, this also confirms the accuracy of considering mechanical dynamics in DFIG impedance modeling from the side.

B. Application of CIM in Stability Analysis of Grid-Connected Wind Farm System

It is worth noting that the grid impedance significantly affects the stability of grid-connected wind farm systems. Therefore, this section takes into account grid impedance and analyzes wind farm stability using the proposed CIM. The grid side beyond the wind farm PCC can be represented as an RL equivalent circuit, with its *dq*-frame impedance denoted as $\boldsymbol{Z}_{\mathrm{grid}}$. The stability analysis of a grid-connected wind farm system employs the GNC to examine whether the eigenvalues of impedance ratio $\boldsymbol{L} = \boldsymbol{Z}_{\mathrm{grid}}/\boldsymbol{Z}_{\mathrm{farm}}$ satisfy the Nyquist criterion.

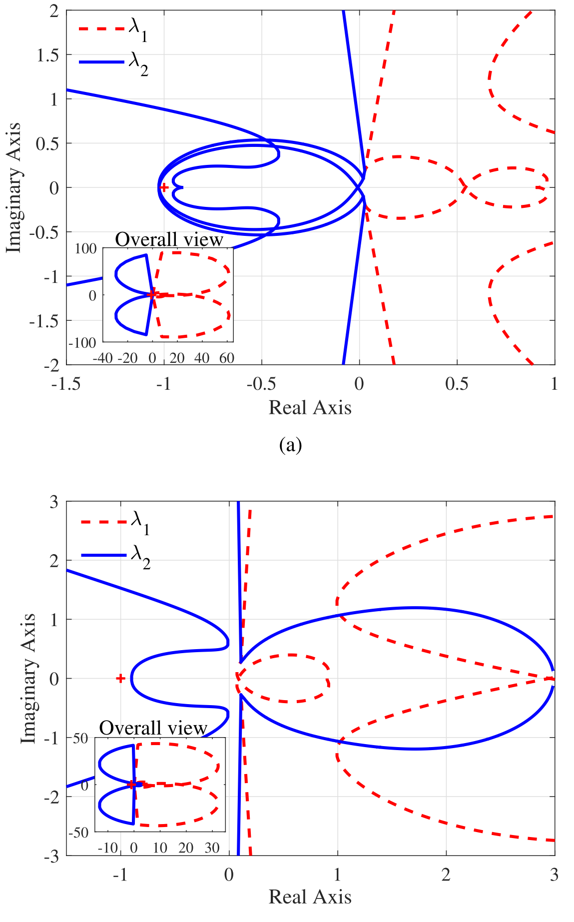

(a)

(b)

Fig. 11. Comparison of GNC diagrams based on different wind farm impedance. (a) Comprehensive impedance with mechanical and WFC dynamics. (b) Simplified impedance without mechanical and WFC dynamics.

The grid impedance parameters are configured to achieve a short-circuit ratio (SCR) of 2.5, indicating a weak grid condition. The power demand commands of the wind farm are set at 15 MW and 0 MVar. Fig. 11(a) illustrates the eigen-trajectories of the CIM-based impedance ratio for the grid-connected wind farm system. It can be observed that eigen-trajectory λ_2 encircles the point $(-1, 0)$, indicating an unstable system state. In contrast, the simplified wind farm impedance, which is based on series-parallel aggregation and does not consider mechanical and WFC dynamics, is used to assess the stability of the grid-connected system. The corresponding GNC diagram is shown in Fig. 11(b). In this case, none of the eigen-trajectories encircle the point $(-1, 0)$, suggesting system stability. This difference in stability analysis results aligns with the fact that both Z_{qd} and Z_{qq} of the CIM exhibit a wider negative resistive behavior compared to those of simplified impedance, as depicted in Fig. 8.

1) Varying the Grid Strength: Keeping the basic parameters and the power demand commands of the wind farm constant, the SCR is increased to 2.6 to enhance grid strength. According to existing analyses, the GNC diagram based on the simplified wind farm impedance will move further away from the point $(-1, 0)$ with increased grid strength, indicating improved system stability. Therefore, the GNC diagram corresponding to the simplified impedance model is no longer given. Instead, the GNC diagram corresponding to the wind farm CIM is presented in Fig. 12. It is observed that after increasing the SCR, the eigen-trajectories no longer encircle the point $(-1, 0)$, and the system becomes stable. This confirms that the proposed wind farm CIM can effectively validate the conclusion that stronger grid strength results in enhanced system stability.

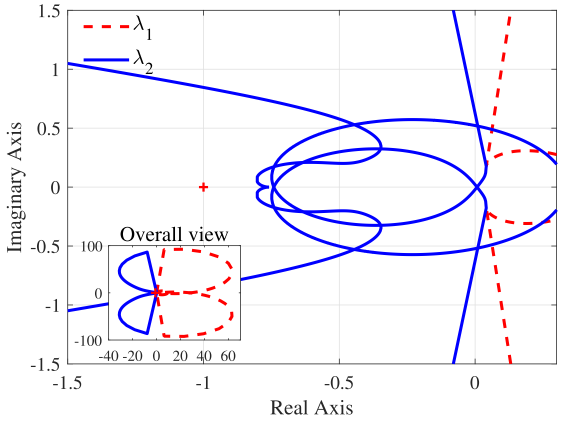

Fig. 12. GNC diagram with increased SCR.

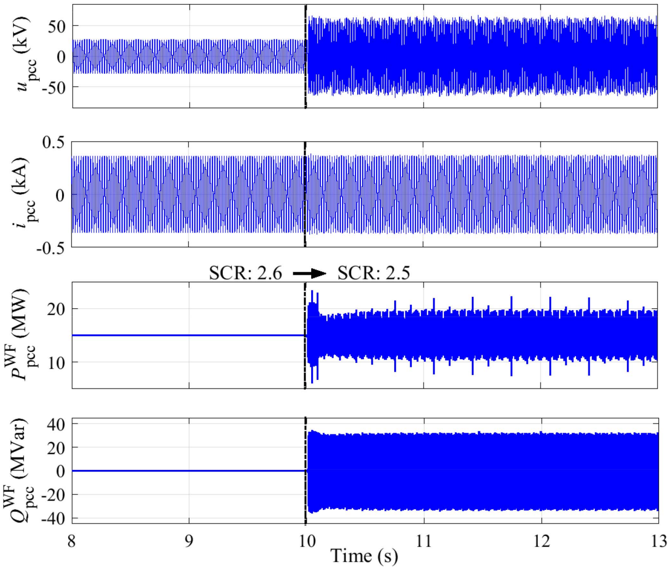

Fig. 13. Simulation results at the wind farm PCC with varying grid strength.

The stability analysis results for the grid-connected wind farm system under different SCRs are verified through MATLAB/Simulink simulation. Throughout the simulation, the output power of the wind farm is maintained at 15 MW and 0 MVar. The SCR is reduced from 2.6 to 2.5 at 10 s. The simulation results are shown in Fig. 13. It is evident from the figure that the system transitions from a stable to an unstable state with the decrease in SCR. This is consistent with the results of the CIM-based GNC, underscoring the accuracy of the wind farm CIM in comparison to the simplified impedance model for stability analysis.

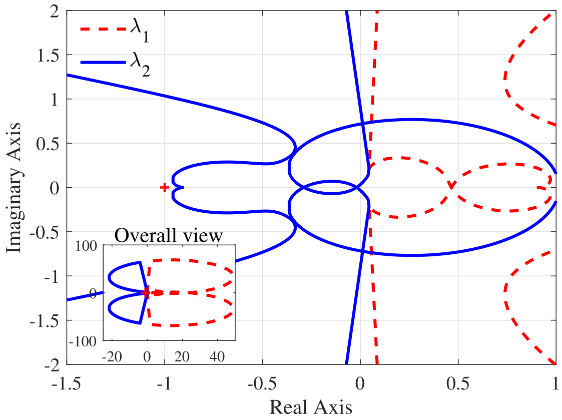

Fig. 14. GNC diagram with reduced WFC PI parameters.

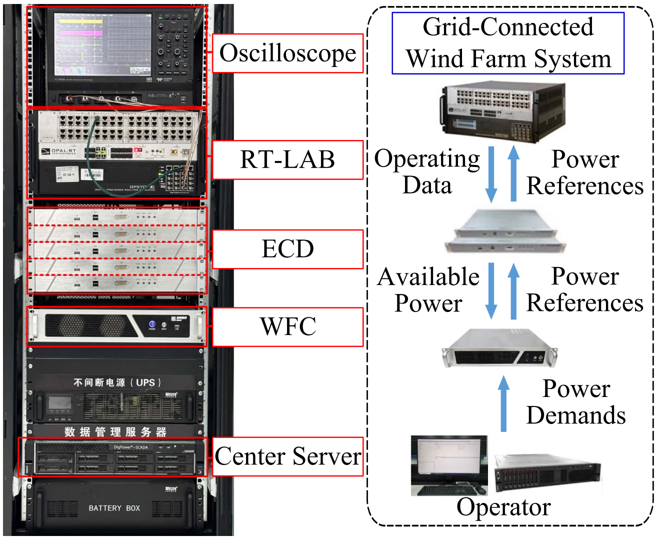

Fig. 15. Configuration of the CHIL experimental platform.

2) Varying the WFC PI Parameter: The SCR of the grid-connected wind farm system is kept at 2.5, while the WFC PI parameters are reduced to $k_{\mathrm{p,WFC}} = 0.1$ and $k_{\mathrm{i,WFC}} = 1$. Since the simplified impedance model of the wind farm does not consider the WFC, and there is no alteration in steady-state operating points of the system, the GNC diagram corresponding to the simplified impedance model remains the same as Fig. 11(b). However, the GNC diagram corresponding to the CIM is changed to Fig. 14. It can be observed that after reducing WFC PI parameters, eigen-trajectories no longer encircle the point $(-1, 0)$, and the system becomes stable. This finding is consistent with the analysis of the influence of WFC PI parameters on wind farm impedance characteristics, as discussed in Section IV-C.

The stability analysis of the grid-connected wind farm system is validated on the controller-hardware-in-loop (CHIL) experimental platform, as depicted in Fig. 15. The WFC is implemented through an external hardware device to effectively validate the analytical conclusions concerning the WFC in this article. Except for the WFC, the simulation model of the grid-connected wind farm system, including the DFIG control, is performed on RT-Lab. The wind farm operating data is first transmitted to the edge computing device (ECD), which includes the wind speed of DFIGs and the root mean square values of the wind farm PCC voltage and current. The ECD is equipped with an Intel Celeron N3350 CPU, responsible for real-time computation of the available power of each DFIG and the wind farm PCC power. Subsequently, the ECD forwards this data to the WFC. At the same time, the WFC receives power demand commands from the center server for wind farm power control and then communicates power references to each DFIG. Data communication among these devices is achieved using the user datagram protocol.

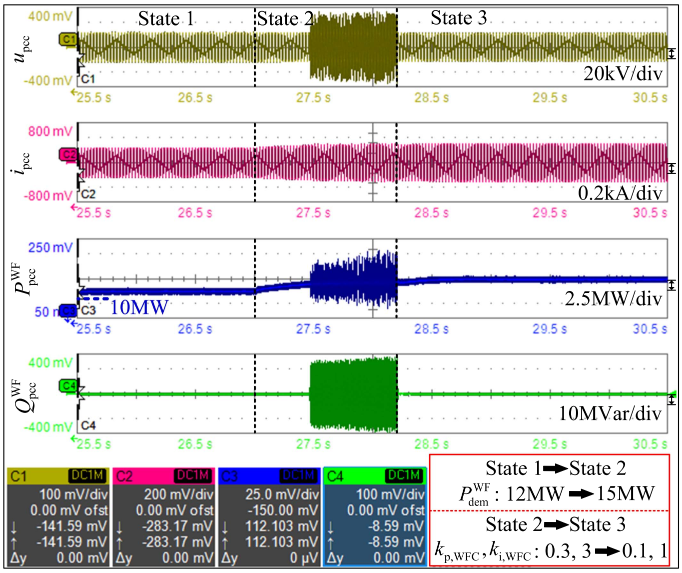

Fig. 16. Experimental results at the wind farm PCC.

Initially, the wind farm operates at an output power of 12 MW and 0 MVar, demonstrating stable operation. The wind farm active power demand command is increased to 15 MW at 27 s. The experimental results at the wind farm PCC are presented in Fig. 16. It can be observed that the system exhibits oscillations following the increase in active power. This phenomenon aligns with the analysis results of CIM-based GNC, further confirming the accuracy of wind farm CIM. Moreover, it also indicates that wind farm CIM demonstrates superior performance in stability analysis, thereby enhancing the precision of stability assessments. At 28.2 s, the WFC PI parameters are reduced to $k_{\mathrm{p,WFC}} = 0.1$ and $k_{\mathrm{i,WFC}} = 1$. From Fig. 16, it can be seen that the system gradually returns to a stable operation state after reducing the WFC PI parameters. This is consistent with the GNC analysis results shown in Fig. 14, verifying the conclusion that excessively large WFC PI parameters make the grid-connected wind farm system more susceptible to instability.

VI. CONCLUSION

This article presents a wind farm CIM to analyze the impedance characteristics of multiple dynamic couplings within the wind farm. The wind farm CIM incorporates the small-signal characteristics of the DFIG rotor speed and the WFC, effectively capturing the dynamic couplings between the WFC, WTs, and collector lines. Comparative analysis reveals that mechanical dynamics significantly impact the low-frequency characteristics of the DFIG impedance, which cannot be neglected when analyzing low-frequency power oscillations. In addition, the WFC dynamics influence wind farm impedance characteristics in the full-frequency range by facilitating couplings between WTs and collector lines throughout the wind farm. The correctness of the proposed CIM is verified through simulation measurements. Furthermore, the superior performance of the wind farm CIM in stability analysis is evaluated through the GNC and confirmed through the CHIL experiment. Moreover, impedance analysis of the CIM demonstrates that excessively large WFC PI parameters can increase susceptibility to instability in the grid-connected wind farm system, which is supported by experimental results.

The CIM formulates the modeling standard of the wind farm impedance and provides the mathematical representation for stability analysis of the grid-connected wind farm system. In the future, the reduced-order model will be investigated based on the work of this article to solve the problem of complex calculation of full-order wind farm impedance.

APPENDIX A
IMPEDANCE MODELING OF GSC PART

The impedance model for the GSC control is given by

$$\Delta \boldsymbol{u}_{\mathrm{g}}^{\mathrm{c}} = \boldsymbol{Z}_{\mathrm{gsc,u}} \begin{bmatrix} \Delta u_{\mathrm{dc}} \\ 0 \end{bmatrix} + \boldsymbol{Z}_{\mathrm{gsc,ig}} \Delta \boldsymbol{i}_{\mathrm{g}}^{\mathrm{c}} \tag{51}$$

$$\boldsymbol{Z}_{\mathrm{gsc,u}} = \begin{bmatrix} -G_{\mathrm{pi,u}} G_{\mathrm{pi,ig}} & 0 \\ 0 & 0 \end{bmatrix}$$

$$\boldsymbol{Z}_{\mathrm{gsc,ig}} = \begin{bmatrix} -G_{\mathrm{pi,ig}} & -\omega_{\mathrm{s}} L_{\mathrm{g}} \\ \omega_{\mathrm{s}} L_{\mathrm{g}} & -G_{\mathrm{pi,ig}} \end{bmatrix} \tag{52}$$

where $G_{\mathrm{pi,u}} = k_{\mathrm{p,u}} + k_{\mathrm{i,u}}/s$ and $G_{\mathrm{pi,ig}} = k_{\mathrm{p,ig}} + k_{\mathrm{i,ig}}/s$ are the PI transfer functions of the GSC voltage and current control.

The dc voltage perturbations can be derived according to the power of GSC and RSC as

$$\begin{bmatrix} \Delta u_{\mathrm{dc}} \\ 0 \end{bmatrix} = \boldsymbol{Z}_{\mathrm{dc,ig}} \Delta \boldsymbol{u}_{\mathrm{g}}^{\mathrm{s}} + \boldsymbol{Z}_{\mathrm{dc,ug}} \Delta \boldsymbol{i}_{\mathrm{g}}^{\mathrm{s}} + \boldsymbol{Z}_{\mathrm{dc,ir}} \Delta \boldsymbol{u}_{\mathrm{r}}^{\mathrm{s}} + \boldsymbol{Z}_{\mathrm{dc,ur}} \Delta \boldsymbol{i}_{\mathrm{r}}^{\mathrm{s}} \tag{53}$$

$$\begin{aligned}
\boldsymbol{Z}_{\mathrm{dc,ig}} &= -\frac{1.5}{sC_{\mathrm{dc}}U_{\mathrm{dc}}} \begin{bmatrix} I_{\mathrm{gd}}^{\mathrm{s}} & I_{\mathrm{gq}}^{\mathrm{s}} \\ 0 & 0 \end{bmatrix} \\
\boldsymbol{Z}_{\mathrm{dc,ug}} &= -\frac{1.5}{sC_{\mathrm{dc}}U_{\mathrm{dc}}} \begin{bmatrix} U_{\mathrm{gd}}^{\mathrm{s}} & U_{\mathrm{gq}}^{\mathrm{s}} \\ 0 & 0 \end{bmatrix} \\
\boldsymbol{Z}_{\mathrm{dc,ir}} &= -\frac{1.5}{sC_{\mathrm{dc}}U_{\mathrm{dc}}} \begin{bmatrix} I_{\mathrm{rd}}^{\mathrm{s}} & I_{\mathrm{rq}}^{\mathrm{s}} \\ 0 & 0 \end{bmatrix} \\
\boldsymbol{Z}_{\mathrm{dc,ur}} &= -\frac{1.5}{sC_{\mathrm{dc}}U_{\mathrm{dc}}} \begin{bmatrix} U_{\mathrm{rd}}^{\mathrm{s}} & U_{\mathrm{rq}}^{\mathrm{s}} \\ 0 & 0 \end{bmatrix}.
\end{aligned} \tag{54}$$

The small-signal model of the GSC filter in the dq-frame is

$$\Delta \boldsymbol{u}_{\mathrm{g}}^{\mathrm{s}} = \boldsymbol{Z}_{\mathrm{g}} \Delta \boldsymbol{i}_{\mathrm{g}}^{\mathrm{s}} + \Delta \boldsymbol{u}_{\mathrm{s}}^{\mathrm{s}} \tag{55}$$

$$\boldsymbol{Z}_{\mathrm{g}} = \begin{bmatrix} R_{\mathrm{g}} + sL_{\mathrm{g}} & -\omega_{\mathrm{s}} L_{\mathrm{g}} \\ \omega_{\mathrm{s}} L_{\mathrm{g}} & R_{\mathrm{g}} + sL_{\mathrm{g}} \end{bmatrix}. \tag{56}$$

APPENDIX B
PARAMETERS OF DFIG-BASED WIND FARM

TABLE I
PARAMETERS OF DFIG LEVEL

Symbol	Parameter	Value
S_{rated}	Rated power	3 MVA
$u_{\mathrm{s,rated}}$	Stator rated voltage	690 V
u_{dc}	DC voltage	1150 V
C_{dc}	DC capacitance	0.08 F
N	Gearbox ratio	100
p	Pole pairs	2
J	Inertia	127 kg·m^2
ω_{s}	System angular frequency	314 rad/s
f_{sw}	Switching frequency	4 kHz
R_{s}	Stator resistance	2.6 mΩ
L_{s}	Stator inductance	2.6 mH
R_{r}	Rotor resistance	2.9 mΩ
L_{r}	Rotor inductance	2.6 mH
L_{m}	Mutual inductance	2.5 mH
R_{g}	GSC filter resistance	0.02 mΩ
L_{g}	GSC filter inductance	0.4 mH

Control parameters

Parameter	Value	Parameter	Value
$k_{\mathrm{p,PQ}}$	0.001	$k_{\mathrm{i,PQ}}$	0.01
$k_{\mathrm{p,ir}}$	0.18	$k_{\mathrm{i,ir}}$	1
$k_{\mathrm{p,u}}$	–5.92	$k_{\mathrm{i,u}}$	–35.5
$k_{\mathrm{p,ig}}$	3.02	$k_{\mathrm{i,ig}}$	56.85
k_{ppll}	0.32	k_{ipll}	5.68

TABLE II
PARAMETERS OF WIND FARM LEVEL

35kV Branch	Resistance (Ω)	Inductance (mH)
1	0.1056	0.5721
2	0.1590	0.4393
3	0.1844	0.9993
4	0.9615	2.6563
5	0.1946	1.0547
6	0.0971	0.4110
7	0.2229	0.9436
8	0.3665	1.5513
9	0.3923	1.6605
10	0.5541	2.3455
11	0.0125	0.1306

Control parameters

Parameter	Value	Parameter	Value
$k_{\mathrm{p,WFC}}$	0.3	$k_{\mathrm{i,WFC}}$	3

REFERENCES

[1] X. Wang and F. Blaabjerg, “Harmonic stability in power electronic-based power systems: Concept, modeling, and analysis,” *IEEE Trans. Smart Grid*, vol. 10, no. 3, pp. 2858–2870, May 2019.

[2] H. Li, J. Shair, J. Zhang, and X. Xie, “Investigation of subsynchronous oscillation in a DFIG-based wind power plant connected to MTDC grid,” *IEEE Trans. Power Syst.*, vol. 38, no. 4, pp. 3222–3231, Jul. 2023.

[3] Y. Li, L. Fan, and Z. Miao, “Wind in weak grids: Low-frequency oscillations, subsynchronous oscillations, and torsional interactions,” *IEEE Trans. Power Syst.*, vol. 35, no. 1, pp. 109–118, Jan. 2020.

[4] J. Sun, “Impedance-based stability criterion for grid-connected inverters,” *IEEE Trans. Power Electron.*, vol. 26, no. 11, pp. 3075–3078, Nov. 2011.

[5] A. D. Hansen, P. Sørensen, F. Iov, and F. Blaabjerg, “Centralised power control of wind farm with doubly fed induction generators,” *Renewable Energy*, vol. 31, no. 7, pp. 935–951, 2006.

[6] P. Wang, Z. Zhang, Q. Huang, N. Wang, X. Zhang, and W.-J. Lee, “Improved wind farm aggregated modeling method for large-scale power system stability studies,” *IEEE Trans. Power Syst.*, vol. 33, no. 6, pp. 6332–6342, Jun. 2018.

[7] L. Piyasinghe, Z. Miao, J. Khazaei, and L. Fan, “Impedance model-based SSR analysis for TCSC compensated type-3 wind energy delivery systems,” *IEEE Trans. Sustain. Energy*, vol. 6, no. 1, pp. 179–187, Jan. 2015.

[8] Y. Xu, H. Nian, T. Wang, L. Chen, and T. Zheng, “Frequency coupling characteristic modeling and stability analysis of doubly fed induction generator,” *IEEE Trans. Energy Convers.*, vol. 33, no. 3, pp. 1475–1486, Mar. 2018.

[9] F. Shi, D. Shu, Z. Yan, and Z. Song, “A shifted frequency impedance model of doubly fed induction generator (DFIG)-based wind farms and its applications on S^2SI analysis,” *IEEE Trans. Power Electron.*, vol. 36, no. 1, pp. 215–227, Jan. 2021.

[10] Y. Song, X. Wang, and F. Blaabjerg, “Impedance-based high-frequency resonance analysis of DFIG system in weak grids,” *IEEE Trans. Power Electron.*, vol. 32, no. 5, pp. 3536–3548, May 2017.

[11] K. Sun, W. Yao, J. Fang, X. Ai, J. Wen, and S. Cheng, “Impedance modeling and stability analysis of grid-connected DFIG-based wind farm with a VSC-HVDC,” *IEEE J. Emerg. Sel. Topics Power Electron.*, vol. 8, no. 2, pp. 1375–1390, Feb. 2020.

[12] L. Yang, Z. Xu, J. Østergaard, Z. Y. Dong, K. P. Wong, and X. Ma, “Oscillatory stability and eigenvalue sensitivity analysis of a DFIG wind turbine system,” *IEEE Trans. Energy Convers.*, vol. 26, no. 1, pp. 328–339, Jan. 2011.

[13] S. Huang, Q. Wu, W. Bao, N. D. Hatziargyriou, L. Ding, and F. Rong, “Hierarchical optimal control for synthetic inertial response of wind farm based on alternating direction method of multipliers,” *IEEE Trans. Sustain. Energy*, vol. 12, no. 1, pp. 25–35, Jan. 2021.

[14] H. Zhao, Q. Wu, Q. Guo, H. Sun, and Y. Xue, “Distributed model predictive control of a wind farm for optimal active power control part ii: Implementation with clustering-based piece-wise affine wind turbine model,” *IEEE Trans. Sustain. Energy*, vol. 6, no. 3, pp. 840–849, Mar. 2015.

[15] J. Kazda and N. A. Cutululis, “Model-optimized dispatch for closed-loop power control of waked wind farms,” *IEEE Trans. Control Syst. Technol.*, vol. 28, no. 5, pp. 2029–2036, May 2020.

[16] H. Liu, X. Xie, X. Gao, H. Liu, and Y. Li, “Stability analysis of SSR in multiple wind farms connected to series-compensated systems using impedance network model,” *IEEE Trans. Power Syst.*, vol. 33, no. 3, pp. 3118–3128, Mar. 2018.

[17] W. Dong, W. Du, X. Xie, and H. F. Wang, “An approximate aggregated impedance model of a grid-connected wind farm for the study of small-signal stability,” *IEEE Trans. Power Syst.*, vol. 37, no. 5, pp. 3847–3861, May 2022.

[18] B. Gao, Y. Liu, B. Shao, and H. Ran, “A path analysis method to study the subsynchronous oscillation mechanism in direct-drive wind farm with VSC-HVDC system,” *Int. J. Electr. Power Energy Syst.*, vol. 142, 2022, Art. no. 108328.

[19] X. Wang, L. Harnefors, and F. Blaabjerg, “Unified impedance model of grid-connected voltage-source converters,” *IEEE Trans. Power Electron.*, vol. 33, no. 2, pp. 1775–1787, Feb. 2018.

[20] F. Mei and B. Pal, “Modal analysis of grid-connected doubly fed induction generators,” *IEEE Trans. Energy Convers.*, vol. 22, no. 3, pp. 728–736, Mar. 2007.

[21] W. R. E. M. T. Force, “WECC wind plant dynamic modeling guidelines,” in *Western Electricity Coordinating Council Modeling and Validation Work Group*, vol. 17, 2014.

[22] J. Rodriguez-Amenedo, S. Arnalte, and J. Burgos, “Automatic generation control of a wind farm with variable speed wind turbines,” *IEEE Trans. Energy Conver.*, vol. 17, no. 2, pp. 279–284, Feb. 2002.

[23] M. Darabian and A. Bagheri, “Stability improvement of large-scale power systems including offshore wind farms and MTDC grid aiming at compensation of time delay in sending robust damping signals,” *Int. J. Electr. Power Energy Syst.*, vol. 143, 2022, Art. no. 108491.

[24] H. Liu, X. Xie, and W. Liu, “An oscillatory stability criterion based on the unified dq-frame impedance network model for power systems with high-penetration renewables,” *IEEE Trans. Power Syst.*, vol. 33, no. 3, pp. 3472–3485, Mar. 2018.

[25] W. Cao, Y. Ma, L. Yang, F. Wang, and L. M. Tolbert, “D–Q impedance based stability analysis and parameter design of three-phase inverter-based AC power systems,” *IEEE Trans. Ind. Electron.*, vol. 64, no. 7, pp. 6017–6028, Jul. 2017.

[26] C. Du, X. Du, C. Tong, Y. Li, and P. Zhou, “Stability analysis for DFIG-based wind farm grid-connected system under all wind speed conditions,” *IEEE Trans. Ind. Appl.*, vol. 59, no. 2, pp. 2430–2445, Feb. 2023.

[27] B. Wen, D. Boroyevich, R. Burgos, P. Mattavelli, and Z. Shen, “Analysis of D-Q small-signal impedance of grid-tied inverters,” *IEEE Trans. Power Electron.*, vol. 31, no. 1, pp. 675–687, Jan. 2016.

[28] H. Gong, D. Yang, and X. Wang, “Impact analysis and mitigation of synchronization dynamics for DQ impedance measurement,” *IEEE Trans. Power Electron.*, vol. 34, no. 9, pp. 8797–8807, Sep. 2019.

Jinlong Wang (Student Member, IEEE) received the B.S. and M.S. degrees in electrical engineering in 2019 and 2022, respectively, from Shandong University, Jinan, China, where he is currently working toward the Ph.D. degree in electrical engineering.

His research interests include modeling and control of power electronics and stability analysis of power electronics-based power systems.

Peng Wang (Member, IEEE) was born in Shandong, China, in 1988. He received the M.E. degree in electrical engineering from Shandong University, Jinan, China, in 2014 and the Dr.-Ing. (*summa cum laude*) degree in electrical engineering from the Technical University of Berlin, Berlin, Germany, in 2020.

He is currently with the School of Electrical Engineering, Shandong University. In 2018, he was an Electrical Engineer with State Grid Corporation of China, Beijing, China. His research interests include modeling and stability analysis of ac–dc power system integrated with renewable generation.

Haoran Zhao (Senior Member, IEEE) received the B.E. degree in electrical engineering and automation from Shandong University, Jinan, China, in 2005, the M.E. degree in electrical engineering and automation from the Technical University of Berlin, Berlin, Germany, in 2010, and the Ph.D. degree in electrical engineering from the Technical University of Denmark, Kongens Lyngby, Denmark, in 2014.

He is currently a Professor with the School of Electrical Engineering, Shandong University. From 2010 to 2011, he was an Application Developer with DIgSILENT GmbH, Gomaringen, Germany. His research interests include modeling and integration study of wind power, control of energy storage systems, and voltage stability analysis.

Futao Yang received the B.S. degree in computer applications and the M.S. degree in power engineering from Shandong University, Jinan, China, in 1998 and 2006, respectively. He is currently working toward the Ph.D. degree in electrical engineering with Shandong University.

His research interests include renewable power generation and energy storage applications.